

Self-similar spiral flow structure in low Reynolds number isotropic and decaying turbulence

J. C. Vassilicos¹ and James G. Brasseur²

¹*Department of Applied Mathematics and Theoretical Physics, University of Cambridge, Cambridge CB3 9EW, England*

²*Department of Mechanical Engineering, Pennsylvania State University, State College, Pennsylvania 16804*

(Received 9 January 1996)

It is rigorously proved for axisymmetric incompressible flows with bounded axial vorticity at infinity that if a spiral-helical streamline has a Kolmogorov capacity (box-counting dimension) $D_K > 1$, then the velocity field must have a singularity at the axis of symmetry. Furthermore, certain types of singularity with $D_K = 1$ can be excluded. The Burgers and the Lundgren vortices are examples of strained vortices with different types of near-singular structure, and in both cases sections of streamlines have a well-defined $D_K > 1$. However, the strain severely limits the region in space where D_K is larger than 1. An algorithm is developed which detects streamlines with persistently strong curvature and calculates both the D_K of the streamlines *and* the lower bound scale δ_{\min} of the range of self-similar scaling defined by D_K . Error bounds on D_K are also computed. The use of this algorithm partly relies on the fact that two to three turns of a spiral are enough to determine a spiral's D_K . We detect well-defined self-similar scaling in the geometry of streamlines around vortex tubes in decaying isotropic direct numerical simulation turbulence with exceptionally fine small-scale resolution and Re_λ around 20. The measured values of D_K vary from $D_K = 1$ to $D_K \approx 1.60$, and in general the self-similar range of length scales over which D_K is well defined extends over one decade and ends at one of two well-defined inner scales, one just above and the other just below the Kolmogorov microscale η . We identify two different types of accumulation of length scales with $D_K > 1$ on streamlines around the vortex tubes in the simulated turbulence: an accumulation of the streamline towards a central axis of the vortex tube in a spiral-helical fashion, and a helical and axial accumulation of the streamline towards a limit circle at the periphery of the vortex tube. In the latter case, the limit circle lies in a region along the axis of the vortex tube where there is a rapid drop in enstrophy. The existence of spiral-helical streamlines with well-defined $D_K > 1$ suggests the possibility of a near-singular flow structure in some vortex tubes. Finally, we present some evidence based on the spatial correlation of enstrophy with viscous force indicating that the spatial vorticity profile across vortex tubes is not a well-resolved Gaussian at the resolution of the present simulations. [S1063-651X(96)04607-7]

PACS number(s): 47.27.-i

I. INTRODUCTION

Hunt and Vassilicos [1] pointed out that a self-similar energy spectrum $E(k) \sim k^{-2p}$ where p is a noninteger (such as Kolmogorov's $2p = \frac{5}{3}$) implies the existence of near singularities in the turbulent velocity field that cannot simply be isolated discontinuities in the velocities or their derivatives, as in the case of plane vortex sheets. (A near singularity or near-singular flow exhibits the asymptotic structure of a singularity outside a limited friction-dominated region where viscosity smooths out the flow. Near singularities may tend to singularities in the limit where the viscosity $\nu \rightarrow 0$. However, the limit $\nu \rightarrow 0$ for turbulent flows lies outside the scope of the present paper.) These near singularities must fall in one or more of the following three categories: simple near singularities [Fig. 1(a)], complex isolated near singularities [Fig. 1(b)], and nonisolated near singularities [Fig. 1(c)]. However, the precise nature and origin of these near singularities is not known. They could be complex isolated (accumulating) near singularities if, for example, small localized shear layers exist in the turbulence that become unstable and lead to a spiral vortex sheet structure (see Lundgren [2,3]) or simple power-law near singularities [the azimuthal velocity u_ϕ of two-dimensional (2D) inviscid point vortices varies with cylindrical radius r according to $u_\phi \sim r^{-q}$, $q > 0$]. Both of these near-singular flow patterns have a scaling symmetry, or self-similar flow structure, around their centers (see Vas-

silicos and Hunt [4] and Hunt and Vassilicos [1]). Nonisolated singular flow structure could be produced by chaotic advection, for example, of the small scales by the unsteady larger scale motions of the turbulence.

Neither the mixture of simple, complex isolated, and nonisolated near singularities, nor the distribution in space of these near singularities in the turbulence is known, either at low or high Reynolds numbers. The near singularities implied by a self-similar power spectrum (such as Kolmogorov's energy spectrum) must have self-similar scaling properties on average. However, not all imaginable near singularities have such scaling properties. What flow structures in the small-scale turbulence carry near singularities with self-similar scaling properties? Given that near singularities necessarily exist in high Reynolds number turbulence where $E(k) \sim k^{-2p}$ and p is a noninteger, do near singularities also exist in lower Reynolds number turbulence?

Recent laboratory experiments (Cadot, Douady, and Couder [5], Villermeaux, Sixou, and Gagne [6]) and direct numerical simulations (DNS) (see Jiménez *et al.* [7], and references therein) have led to the discovery of strong coherent and elongated vortices among the small scales in a variety of low-to-moderate Reynolds number turbulent flows. In particular, Jiménez *et al.* [7] demonstrated that the strongest vortex tubes are a necessary product of the evolution of both forced and decaying isotropic turbulence. However, the origin and internal structure of these vortex tubes is not yet

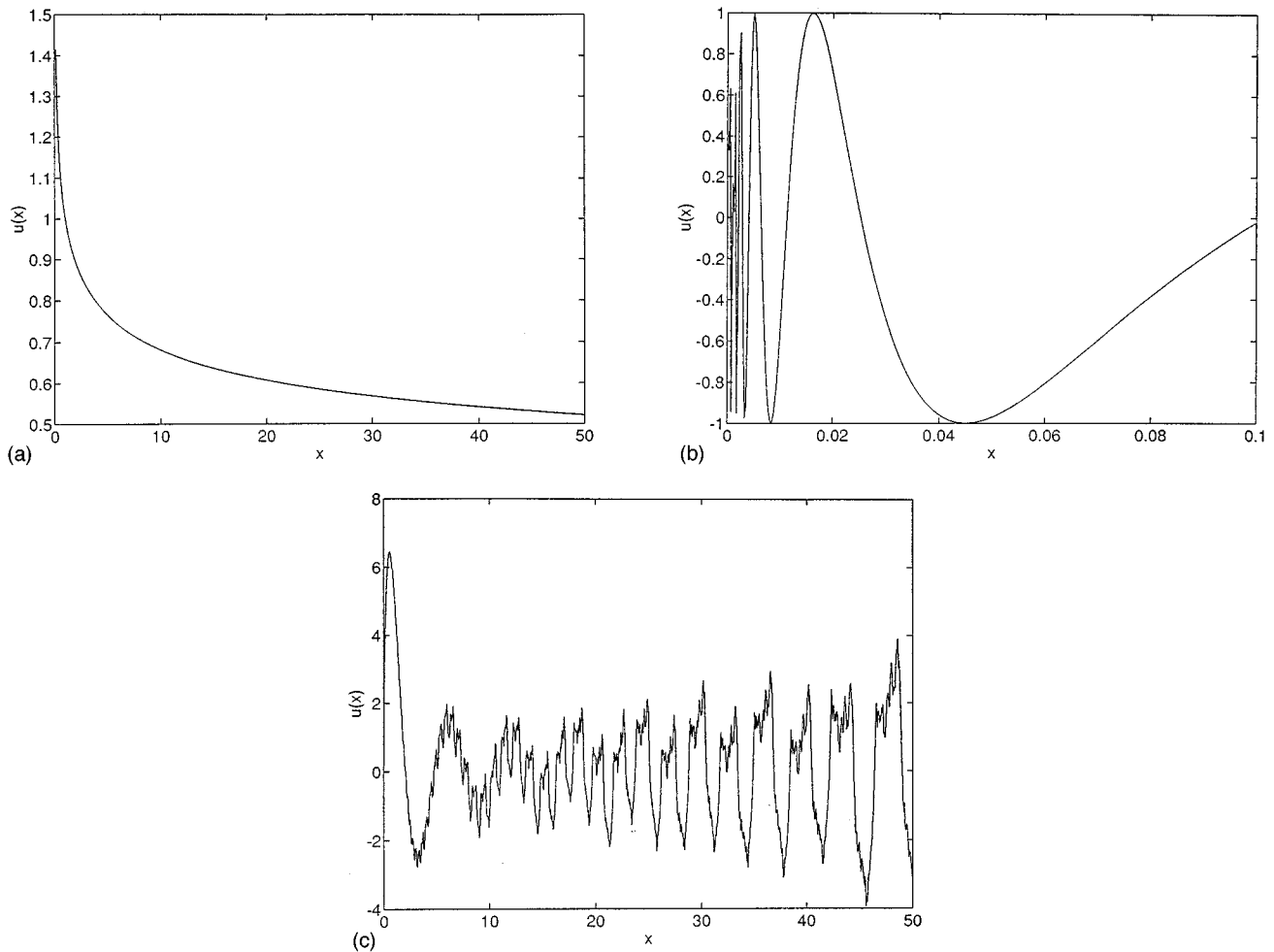


FIG. 1. In 1D, (a) the function $u(x) = x^{-1/6}$ has an energy spectrum $E(k) \sim k^{-5/3}$; (b) the function $u(x) = \sin(x^{-1/2})$ has an energy spectrum $E(k) \sim k^{-5/3}$; (c) the Weierstrass function $u(x) = \sum_{n=0}^{\infty} k_n^{D-2} \sin(k_n x)$ where $k_n = y^n$ with $y > 1$ and $D = \frac{7}{6}$ has an energy spectrum $E(k) \sim k^{-5/3}$.

understood. Two different mechanisms for their formation are currently considered by various workers in the field. The first is that vortex tubes originate from strained vorticity, such as the Burgers vortex, for example. The second is that they are the result of a shear instability leading to a spiral roll-up of vortex sheets. In the first case, a simple velocity near singularity of the r^{-q} type outside a limited friction-dominated region may exist; for example, the azimuthal velocity of the Burgers vortex drops off as r^{-1} outside the vortex core. In the second case, the internal vortex and velocity structures would have a complex isolated near singularity reflected by a spiral distribution of vorticity within a vortex tube. A model for such vortex near singularities is the Lundgren [2,3] strained spiral vortex which is an asymptotic solution of the Navier-Stokes equations for long times.

Attempts to answer questions concerning the existence and nature of near singularities in turbulent flows may be made by recourse to data and with appropriate diagnostic tools. Kevlahan and Vassilicos [8] developed tools based on fractal and wavelet methods which they applied to one-dimensional experimental high Reynolds number turbulence data in an attempt to determine whether and to what extent high Reynolds number turbulence near singularities are isolated (e.g., spiral) or nonisolated (e.g., fractal). With DNS,

we now have access to three-dimensional numerical low-to-moderate Reynolds number turbulence data from which the 3D flow structures where near singularities may be residing can be visualized and quantitatively analyzed. For such data it may be possible to investigate whether near singularities exist in low Reynolds number turbulence, and specifically whether near singularities are manifest by the vortex tubes of the small-scale turbulence. In this study we analyze a succession of identical turbulence velocity fields with increasing small-scale resolution. In particular, we analyze an exceptionally high-resolution (512^3) turbulence simulation at Re_λ (the Taylor microscale Reynolds number) of order 20 with resolved scales below the Kolmogorov scale η . By comparing different resolution simulations of the same turbulence we can confirm results concerning local near-singular flow structure obtained with lower-resolution simulations.

Even with a succession of high-resolution 3D turbulent velocity fields, conventional methods are not sharp enough to adequately detect and analyze flow near singularities, and new tools are needed. In typical well-resolved direct numerical simulations, the grid size is approximately 2η , and vortex tubes typically cover only five to ten grid points across their width. It is therefore neither practical nor fruitful to proceed by trial and error and fit different functional forms to the

velocities and vorticities at these few points or to directly plot these local velocity and vorticity distributions for multitudes of vortices throughout the computational domain in an attempt to directly ascertain internal vortex structure. In fact, such direct tests have already been attempted, with inconclusive results. Vincent and Meneguzzi [9], for example, show a “cut through a typical vorticity tube along a direction perpendicular to its axis” that suggests a spiral vorticity structure, while Jiménez *et al.* [7] plot the “radial vorticity distribution for different cross sections along a typical worm,” “showing that the Gaussian model is at least reasonable. This model is consistent with that of an axially stretched equilibrium Burgers vortex.” Because unambiguous conclusions cannot be drawn from this direct approach, new fluid mechanical measures are needed which are directly sensitive to the asymptotic similarity and near-singularity properties of localized turbulent flow structures, and which can extract such local information from the flow even in simulations with more typical resolutions.

Because of the common occurrence of local axial motions within vortex tubes, caused by straining, for example, typical streamlines inside and around vortex tubes in turbulent flows can be expected to be curves that are spiral in nature. Most smooth or regular curves, and even most regular spiral curves, have trivial integral Kolmogorov capacities (box-counting fractal dimensions). However, there exists a restricted class of regular spirals that have a nonintegral “fractal” dimension or Kolmogorov capacity D_K (see Vassilicos and Hunt [4]). In Sec. II of this paper we prove that axisymmetric incompressible flows with bounded axial vorticity that have spiral-helical streamlines with Kolmogorov capacities strictly larger than 1 *must* have a singularity in the Eulerian velocity field. Hence the Kolmogorov capacity of a spiral-helical streamline surrounding the viscous core of a vortex tube indicates the near-singular structure of the vortex tube itself. For example, self-similar scaling properties of streamlines around a Burgers or a Lundgren vortex reflect their vorticity and strain-rate structure, and the actual nonintegral value of the Kolmogorov capacity D_K of their streamlines is determined by the scaling properties of the near singularity, the details of the straining field, and the Reynolds number.

In this paper we directly identify and systematically analyze vortex tubes using the Kolmogorov capacity of the geometry of individual streamlines associated to vortex tubes as a measure of *local* self-similar scaling and near-singular flow structure. This measure is robust at low Reynolds numbers. We study the self-similarity properties of streamlines around small-scale vortex tubes in isotropic decaying turbulence where the Taylor microscale Reynolds number is $Re_\lambda \approx 20$, too low for a self-similar energy spectrum to exist.

It should be stressed from the onset that we are searching for what may be rare but perhaps significant events. The suggestion of this paper’s fractal analysis of streamlines is that near-singular self-similar flow structure exists around a significant number of local high vorticity regions in low Re decaying turbulence. It is well known, however, that high vorticity regions with vortex tube topology fill only a small percentage of the total domain of the turbulence.

In Sec. III we discuss the DNS data used, the interpolation schemes, and our method of *systematic local* “fractal” analysis, and in Sec. IV we discuss the application of the

procedure to isotropic decaying turbulence and the results. We conclude in Sec. V.

II. THE RELATION BETWEEN THE SELF-SIMILAR SPIRAL GEOMETRY OF STREAMLINES AND THE EULERIAN VELOCITY, VORTICITY, AND STRAIN-RATE FIELDS

From a fluid mechanics point of view, spiral streamlines occur naturally in turbulence around tubelike concentrations of vorticity when pressure forces cause fluid motion along the tube axis. These pressure forces may be associated, for example, with local straining of the vortex tube or local divergence of the vortex lines. The topology of the locally spiraling streamlines is therefore a reflection of the structure of the local vorticity and strain-rate fields.

From a dynamical systems point of view, spirals occur in the vicinity of particular invariant manifolds such as hyperbolic points. Stability analysis can reveal the spiral structure near the manifold, but such analysis being linear, the spiral’s geometry is only known very close to the hyperbolic point where the spiral is logarithmic. Logarithmic spirals, however, have a Kolmogorov capacity $D_K=1$ (see Vassilicos and Hunt [4] for the Kolmogorov capacity of spirals). The existence of streamlines with D_K larger than 1 is therefore a nontrivial proposition which involves regions of space where the nonlinearities of the system cannot be neglected. We investigate here the relation between the Kolmogorov capacities of streamlines and the combination and nature of strain-rate and differential rotation that can cause these capacities to be nontrivial in incompressible flows.

A. Singularities and streamline capacities in axisymmetric incompressible flows

In this section we prove the following statement: *in an axisymmetric incompressible flow with bounded axial vorticity at infinity, if a helical streamline spirals in towards the axis of symmetry with a Kolmogorov capacity strictly larger than 1, then the Eulerian velocity field must have a singularity at a finite location on the axis.*

We derive this result analytically by proving its *converse*, which is *in an axisymmetric incompressible flow with helical streamlines that spiral in towards the axis of symmetry, if the Eulerian velocity field is regular (no singularities) near the axis of symmetry and the axial component of the vorticity is bounded near the axis at infinity, then the Kolmogorov capacity of these streamlines must be $D_K=1$.*

In detail, the assumptions of this converse statement follow.

(1) *Axisymmetry and incompressibility*, which imply the existence of a Stokes stream function $\psi(r,z)$ that is independent of the azimuthal cylindrical angle ϕ and only depends on the cylindrical coordinates r (distance from the axis of symmetry) and z (distance along the axis of symmetry). The radial and axial cylindrical velocity components are, respectively,

$$u_r = -\frac{1}{r} \frac{\partial}{\partial z} \psi, \quad (2.1a)$$

$$u_z = \frac{1}{r} \frac{\partial}{\partial r} \psi. \tag{2.1b}$$

(2) *Regularity of the velocity field as $r \rightarrow 0$ for all values of z , and at any small value of r as z is varied.* This means that as $r \rightarrow 0$,

$$\psi(r, z) \approx r^l F(z), \tag{2.2}$$

and the azimuthal velocity component

$$u_\phi(r, z) \approx r^m G(z), \tag{2.3}$$

where F and G are regular functions of z at all noninfinite values of z , and $m \geq 1$ for regularity and incompressibility; the regularity of u_r and u_z requires that $l \geq 2$. However, the minimum requirement on m and l for the present proof to be valid is not regularity of the velocity field, but the weaker requirement that m and l be real numbers such that $(m+1)/l > 0$ and $l > 0$. We state our assumptions in terms of regularity for the sake of simplicity of exposition, but the actual assumptions are even weaker than that. This is made clear in what follows.

From (2.1)–(2.3), the z and r components of a streamline are related by $dr/dz = u_r/u_z \approx -rF'(z)/lF(z)$ as $r \rightarrow 0$ [$F'(z) = (dF/dz)(z)$], which, provided $F(z)$ does not vanish, implies that

$$(r/r_0)^l [F(z)/F_0] \approx 1 \tag{2.4}$$

as $r \rightarrow 0$ (r_0 and F_0 are constants that depend on the particular streamline).

(3) *Existence of helical streamlines that spiral in towards the axis of symmetry of the flow and remain helical arbitrarily close to this axis.* As explained in the next paragraph, this assumption implies that $F(z) \neq 0$ for all z greater than, say, $z=0$, and hence guarantees the validity of (2.4) for $z > 0$. Let us first point out that as the limit $r \rightarrow 0$ is taken on particular helical streamlines that spiral into the axis of symmetry, (2.4) implies that $F(z)$ must tend monotonically towards infinity (because $l > 0$). This monotonic increase in $F(z)$ is not possible unless $z \rightarrow \infty$ since $F(z)$ is a regular function of z at all noninfinite values of z . Hence $F(z)$ must be a monotonically increasing function of z .

If F does vanish at, say, $z=0$, its regularity implies that $F(z) \approx Cz^b$ as $z \rightarrow 0$, where C is a constant and the exponent b is a strictly positive integer ($b \geq 1$). Near $z=0$ and as $r \rightarrow 0$, $u_r \approx -bCr^{l-1}z^{b-1}$ and $u_z \approx lCr^{l-2}z^b$. Considering the four possibilities based on whether C is positive or negative and b even or odd, streamlines either move away from $z=0$ and towards the axis of symmetry or towards $z=0$ and away from the axis of symmetry. In the plane $z=0$, streamlines may spiral in towards the axis without leaving the plane $z=0$ and therefore without being helical. Since we assume that a streamline exists which spirals in towards and is helical arbitrarily close to the central axis, $F(z)$ must remain different from 0 along that streamline when the streamline is sufficiently close to the axis; (2.4) is valid over that region where the streamline is spiraling close to the axis.

Another consequence of the streamline's spiraling towards the axis is that the azimuthal angle's (ϕ) variation along the streamline is such that ϕ increases with increasing

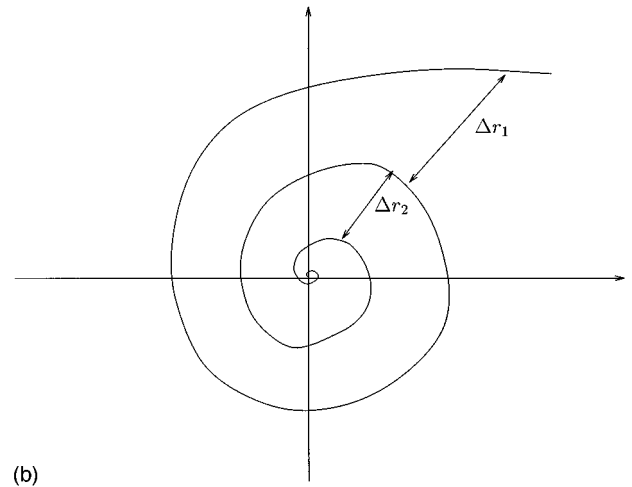
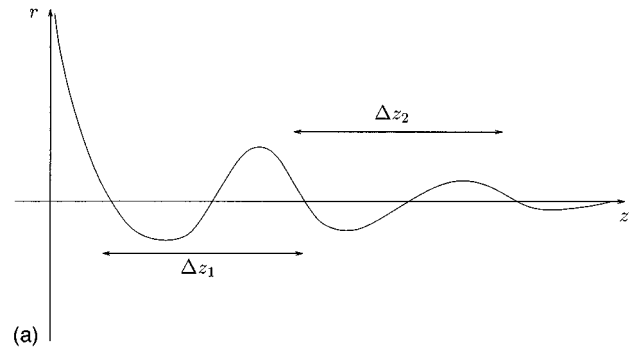


FIG. 2. Schematic drawings of (a) the projection of a spiral-helical streamline on an axial plane, and (b) the projection of the same streamline on the azimuthal plane.

z and decreasing r . The derivative $d\phi/dr$ taken along the streamline is therefore strictly negative; because $F'(z) > 0$ for $z > 0$ and because the streamline's projection on the azimuthal plane obeys

$$\frac{d\phi}{dr} = \frac{u_\phi}{ru_r} \approx -r^{m-l} \frac{G(z)}{F'(z)} \tag{2.5}$$

as $r \rightarrow 0$, $G(z)$ must be strictly positive for $z > 0$.

(4) *Boundedness of the axial component of the vorticity near the axis at infinity.* The axial component of the vorticity $\omega_z \approx (m+1)r^{m-1}G(z)$ as $r \rightarrow 0$, and its boundedness implies that $G(z)$ is bounded as $z \rightarrow \infty$.

We now show that the Kolmogorov capacity of the spiral streamline is $D_K = 1$. In Fig. 2(a) we plot the streamline's projection on an axial plane. From the n th to the $(n+1)$ th turn of the streamline [i.e., the streamline's ϕ varies from $n2\pi$ to $(n+1)2\pi$] the streamline's z coordinate changes by an amount $\Delta z_n = z_{n+1} - z_n$. The distance between two successive turns of the spiral streamline in 3D space is $\Delta_n = \sqrt{(\Delta r_n)^2 + (\Delta z_n)^2}$, where Δr_n is the distance between consecutive turns of the streamline's projection on the azimuthal plane [see Fig. 2(b)]. The Kolmogorov capacity D_K of the streamline beyond $z=0$ is equal to 1 if there is no accumulation of length scales (Vassilicos and Hunt [4]). An accumulation of length scales means that Δ_n should tend to 0

as $n \rightarrow \infty$. The streamline's spiraling towards the axis implies that $\Delta r_n \rightarrow 0$ as $n \rightarrow \infty$. However, the boundedness of $G(z)$ as $z \rightarrow \infty$ combined with the fact that $F(z) \rightarrow \infty$ as $z \rightarrow \infty$ implies that $\Delta z_n \rightarrow \infty$ as $n \rightarrow \infty$. Indeed, from (2.4) and (2.5) it follows that

$$2\pi = \int_{n2\pi}^{(n+1)2\pi} d\phi \approx - \int_{r_n}^{r_{n+1}} dr r^{m-1} \frac{G(z(r))}{F'(z(r))} \approx \frac{(F_0 r_0^l)^{\beta-1}}{l} \int_{z_n}^{z_{n+1}} dz \frac{G(z)}{F^\beta(z)} \quad (2.6)$$

as $r \rightarrow 0$, where $\beta = (m+1)/l > 0$. Because $G(z)/F^\beta(z)$ is a decreasing positive function of z , (2.6) can only be satisfied if $\Delta z_n \rightarrow \infty$ as $n \rightarrow \infty$. Hence $\Delta_n \rightarrow \infty$ as $n \rightarrow \infty$, no accumulation of scales exists, and therefore $D_K = 1$. [Strictly speaking, this conclusion only requires that $G(z)$ does not increase with z at a rate faster than $F^\beta(z)$.]

Intuitively, the above argument may be stated as follows: because the flow field is regular and incompressible, it takes the form (2.2), (2.3), and the helical-spiral streamline must spiral in towards the axis but also towards ever increasing values of z ; and because the axial component of vorticity is bounded at large values of z , the axial motion is much faster than the azimuthal motion, which implies that Δz_n must also increase indefinitely as $n \rightarrow \infty$. Hence there is no accumulation of length scales, even though the streamline is spiral and converges towards the axis, and therefore $D_K = 1$.

Note that this proof does not require that m be larger than or equal to 1; it is only required that $\beta = (m+1)/l$ and l be strictly positive. Hence there exist *singular* Eulerian flow fields where spiral streamlines do *not* have a D_K larger than 1; for example, (2.2) and (2.3) with negative real values of m such that $m > -1$ and $l > 0$.

We now consider an example of an axisymmetric and incompressible near-singular Eulerian flow field which *does* give rise to streamlines with $D_K > 1$ in certain regions local to the vortex if the Reynolds number is large enough, and where the effect of strain is to reduce the Kolmogorov capacity from $D_K > 1$ towards 1 in other regions local to the vortex. In the Appendix we discuss an example of a nearly axisymmetric incompressible flow field with a ‘‘complex’’ (spiral) vorticity singularity.

B. The Burgers vortex:

An axisymmetric ‘‘simple’’ velocity near singularity ($l=2$, $m=-1$), and the effects of strain and Reynolds number on D_K

The Burgers vortex (Burgers [10]) is often used as a model for small-scale turbulence and is an exact steady solution of the Navier-Stokes equations where the continuous action of strain and viscous diffusion balance to give a vortex core of steady, finite size. It has a self-similar energy spectrum $E(k) \sim k^{-1}$ for k small [specifically $E(k) \propto \gamma^2 k^{-1} e^{-(Rk)^2}$ in terms of quantities defined below] which reflects the near-singular behavior of the velocity field outside the vortex core.

In cylindrical coordinates (r, ϕ, z) , the velocity is along the z direction with magnitude

$$\omega(r) = \frac{a \operatorname{Re}_\gamma}{4\pi} e^{-ar^2/4\nu}, \quad (2.7)$$

where ν is the kinematic viscosity, $\operatorname{Re}_\gamma = \gamma/\nu$, and γ is the circulation of the vortex, specifically $\gamma = 2\pi \int_0^\infty \omega(r) r dr$. This flow is sustained by an external straining velocity field derived from the Stokes stream function $\psi = (a/2)r^2 z$ in which a is the strain rate:

$$u_z = az, \quad (2.8a)$$

$$u_r = -\frac{ar}{2}. \quad (2.8b)$$

Vorticity arises from the azimuthal velocity component

$$u_\phi(r) = \frac{\gamma}{2\pi r} (1 - e^{-r^2/2R^2}), \quad (2.8c)$$

where $R = \sqrt{2\nu/a}$ is the radius of the vortex core. Note that $l=2$ [compare $\psi = (a/2)r^2 z$ with (2.2)], and that u_ϕ is singular outside the core where $2\pi u_\phi \approx \gamma/r$, so $m = -1$ [see (2.3)]. The Burgers vortex is an example of an axisymmetric near-singular vortex where streamlines exist with $D_K > 1$; $m = -1$ is marginally outside the domain of validity of the result in Sec. II A that $D_K = 1$ when $\beta = (m+1)/l > 0$ and $l > 0$.

The streamlines of the Burgers vortex are helical around the z axis and spiral in the (r, ϕ) plane with a projection in that plane given by

$$\frac{d\phi}{dr} = -\frac{\gamma}{\pi ar^3} (1 - e^{-r^2/2R^2}). \quad (2.9)$$

A streamline starting at a distance r_0 that is larger than the vortex core radius R revolves around the core n_c times before reaching the core at $r=R$, and

$$n_c \leq \frac{\operatorname{Re}_\gamma}{8\pi^2} \left[1 - \left(\frac{R}{r_0} \right)^2 \right]. \quad (2.10)$$

Clearly, Re_γ needs to be fairly large if there is to be a significant number of revolutions before the streamline enters the core. When this is the case, the streamline's projection on the (r, ϕ) plane takes the spiral form $r(\phi) \sim \phi^{-1/2}$ outside the core, and its Kolmogorov capacity is given by $D_{K\text{proj}} = 1 + \frac{2}{3}$ [from a direct application of the formula $D_K = 1 + 1/(1+b)$ for spirals $r(\phi) \sim \phi^{-b}$, $b > 0$, which is valid when the number of turns of the spiral is not more than roughly four to five turns]; however, if the spiral has more than four to five turns, in which case $D_K = \max(1, 2/(1+b))$ (see Vassilicos and Hunt [4]), then $D_{K\text{proj}} = \frac{4}{3}$. For moderate values of Re_γ where $n_c < 1$, the streamlines rapidly shoot into the vortex core, nearly as straight lines. Inside the vortex core, the streamlines are logarithmic spirals given by

$$r(\phi) \sim e^{-(4\pi/\operatorname{Re}_\gamma)\phi}, \quad (2.11)$$

and the Kolmogorov capacity of the streamline's projection on the (r, ϕ) plane is $D_{K\text{proj}} = 1$.

Note that a $D_{K\text{proj}}$ larger than 1 detects that region *outside* the vortex core where u_ϕ is *singular*. Conversely, $D_{K\text{proj}} = 1$ *inside* the vortex core where $u_\phi \sim r$.

The Kolmogorov capacities of a streamline in 3D space and of its projection in the (r, ϕ) plane are not the same, in general. For a steady Burgers vortex, streamlines and fluid particle paths coincide, and a streamline's coordinates r and z depend on the parameter time t as $z(t) = z_0 e^{at}$ and $r(t) = r_0 e^{-(a/2)t}$, where z_0, r_0 are the coordinates at $t=0$. For large enough values of z_0 , the Kolmogorov capacity of the streamline is $D_K = 1$ because the velocities in the axial direction are much higher than the velocities in the radial direction. Indeed, when the displacement in z after one turn of the spiral streamline is larger than the displacement in r , i.e., when $\Delta z_n > \Delta r_n$ (see Fig. 2), then $D_K = 1$ because the covering with boxes of the 3D streamline is a serial covering—a covering where each box (provided its size is not too large) covers only a portion of *one* coil of the helical spiral and no more (see Vassilicos and Hunt [4] and the box-counting algorithm in Sec. III).

In fact, since $m = -1$ ($\beta = 0$), $\Delta_n = \sqrt{(\Delta r_n)^2 + (\Delta z_n)^2}$ decreases initially and then increases with increasing n , leading to an accumulation of length scales in a restricted region of space where z_0 is sufficiently small. There, the streamlines have a Kolmogorov capacity $D_K = D_{K\text{proj}}$. If r_0 is far inside the vortex core ($r_0 \ll R$), $D_K = 1$, whereas if r_0 is far outside the vortex core ($r_0 \gg R$), then $D_K > 1$ provided that the box counting is limited to the region where the displacement in z after one turn of the spiral is smaller than the displacement in r (i.e., $\Delta z_n \ll \Delta r_n$). In this region

$$z_0 < \frac{r_0}{8\pi^2 r_0^2 / \text{Re}_\gamma R^2 + 1 + \sqrt{8\pi^2 r_0^2 / \text{Re}_\gamma R^2 + 1}}, \quad (2.12)$$

and the 3D spiral streamline may be covered by the same number of boxes as its projection; hence $D_K = D_{K\text{proj}}$. Note that inequality (2.12) implies that the probability of finding a section of streamline with $D_K = D_{K\text{proj}}$ outside the vortex core decreases with decreasing Re_γ . We stress the conclusion that the persistent straining action severely limits the region around the vortex where $D_K > 1$.

For the Burgers vortex to display spiral streamlines with $D_{K\text{proj}} > 1$, and therefore $D_K > 1$ in a restricted region of space, Re_γ should be larger than at least 200 so that streamlines have at least two turns outside the vortex core—from (2.10); two turns is the minimal requirement for D_K to be measurable (Vassilicos and Hunt [4]). For such values of Re_γ to exist in DNS's requires a much larger Reynolds number than what we analyze in this paper. Jiménez *et al.* [7] calculated typical values of Re_γ by fitting a Gaussian distribution of vorticity to the vortex tubes in isotropic simulations of turbulence (as is the case of Burgers vortex tubes). They found that Re_γ grows with Re_λ , and for a forced turbulence of $\text{Re}_\lambda = 35.8$, they found an average value of Re_γ equal to 97, with a standard deviation of about 40 (determined from an inspection of Fig. 10 in Jiménez *et al.* [7]). The maximum values of Re_γ that Jiménez *et al.* [7] observe in their low Reynolds number forced turbulence lie between 150 and 200. We conclude, therefore, that if the vortices in their simulations were Burgers vortices, the probability of detecting streamlines with $D_K > 1$ would be very small.

This conclusion is even stronger for the simulations analyzed here where $\text{Re}_\lambda \approx 20$. Based on the vortex Reynolds numbers measured by Jiménez *et al.* [7], Re_γ should be well below 200 for almost all vortex tubes in the simulations analyzed here. If the turbulence vortex tubes in our simulations are Burgers vortices, it should be very unlikely to find streamlines with more than two turns and $D_K > 1$ in 3D space—see (2.10). As shown in Sec. IV, however, we find a significant number of high-intensity vortex tubes in our simulations that have spiral streamlines with $D_K > 1$, suggesting that these high-intensity vortex tubes in the isotropic turbulence are not Burgers vortices. Furthermore, because the probability of finding streamlines in our simulations with nontrivial Kolmogorov capacities is not small, it appears that many vortex tubes are not subjected to persistent straining, which would severely limit the spatial regions with $D_K > 1$.

The object of the following Secs. III and IV is to demonstrate that spiral-helical streamlines with well-defined nonintegral Kolmogorov capacities do exist around small-scale vortex tubes in DNS low Reynolds number isotropic and decaying turbulence. In fact, the analysis reported in Secs. III and IV leads to the detection of two different types of streamlines with well-defined nonintegral Komogorov capacities D_K ; helical-spiral streamlines accumulating towards a central axis and streamlines with a helical and axial accumulation towards a limit circle.

III. THE FOUR DATA SETS, INTERPOLATION TECHNIQUES, AND THE METHOD OF SYSTEMATIC FRACTAL ANALYSIS

A. The four data sets

We use the numerically generated data set of isotropic unforced decaying turbulence which Yeung and Brasseur [11] obtained by DNS on a 128^3 grid with $\text{Re}_\lambda = 19$, and three other data sets at nearly the same decaying state on 128^3 , 256^3 , and 512^3 grids, respectively, with $\text{Re}_\lambda = 21$. Yeung and Brasseur [11] allowed an initial Gaussian velocity field with a k^2 small wave-number and a $k^{-5/3}$ large wave-number energy-spectrum to evolve by the unforced Navier-Stokes equations until it reached a non-Gaussian equilibrium state of power-law decay. The first velocity field analyzed in this paper is the one that Yeung and Brasseur [11] used as the initial condition in their subsequent forcing calculations. The second 128^3 velocity field analyzed in this paper was obtained from the same initial realization of a Gaussian velocity field with the same initial energy spectrum and the same parameter setting. We refer to the first velocity field by F128 and to the second by S128. These two velocity fields are obtained at slightly different evolution times, resulting in a small difference in Reynolds number. In both data sets the turbulence has evolved several eddy turnover times to a state of power-law decay and the Kolmogorov-scaled high wave-number energy spectrum has collapsed to a single curve. The initial artificial Kolmogorov $-\frac{5}{3}$ spectrum progressively disappears during these simulations.

For the F128 and S128 data sets, the grid spacing $\Delta x \approx 1.8\eta$ [where $\eta = (\nu^3/\epsilon)^{1/4}$ and ϵ is the mean dissipation rate at those times, and $\Delta x k_{\text{max}} \approx \pi$ where k_{max} is the simulation's largest excited wave number] and the longitudinal Taylor

TABLE I. Characteristics of the 4 DNS data sets.

	F128	S128	S256	S512
$\Delta x/\eta \approx$	1.8	1.8	0.92	0.46
$k_{\max}\eta \approx$	1.63	1.61	3.20	6.38
$\text{Re}_\lambda \approx$	19	21	21	21
$\lambda/\Delta x \approx$	5	5	9.8	19.4
$L_p/\Delta x \approx$	11	12.4	25	49.5

microscale $\lambda \approx 5\Delta x$. The longitudinal integral length scale $L_p \approx 11\Delta x$ in the F128 data set with $\text{Re}_\lambda = 19$, and $L_p \approx 12.4\Delta x$ in the S128 data set with $\text{Re}_\lambda = 21$. More information about these data sets can be found in Yeung and Brasseur [11].

As indicated in Table I, the two remaining data sets, S256 and S512, are identical in parameter setting, initial conditions, Reynolds number, and evolution time to S128 but are better resolved because they have been obtained from the unforced evolution of the Navier-Stokes equations on 256^3 and 512^3 grids, respectively. Whereas $k_{\max}\eta = 1.61$ in S128, $k_{\max}\eta = 3.20$ in S256 and $k_{\max}\eta = 6.38$ in S512. In S256 $\Delta x \approx 0.92\eta$, $\lambda \approx 9.8\Delta x$, and $L_p \approx 25\Delta x$, and in S512, $\Delta x \approx 0.46\eta$, $\lambda \approx 19.4\Delta x$, and $L_p \approx 49.5\Delta x$. The analyses were carried out in 128^3 subdomains of the S256 and S512 data sets, corresponding to $\frac{1}{8}$ and $\frac{1}{64}$ of the computational domains, respectively.

B. Interpolation of velocities between nodes and the calculation of streamlines

To calculate instantaneous streamlines, we solve

$$\frac{d\mathbf{x}}{dt} = \mathbf{u}(\mathbf{x}(t)) \quad (3.1)$$

numerically, where $\mathbf{u}(\mathbf{x})$ is the frozen Eulerian velocity field at a point \mathbf{x} . For any given initial position \mathbf{x}_0 , the trajectory $\mathbf{x}(t, \mathbf{x}_0)$ of a fluid element in this frozen velocity field is a streamline and a solution of (3.1).

We used a standard fourth-order Runge-Kutta routine to solve (3.1) with a fictitious time step $\delta t = T_E/200$, where T_E is the Eulerian integral time scale, and the Courant number $\delta t u_{\max}/\Delta x = 0.2$, which is significantly less than 1 (u_{\max} is the maximum value of the three velocity components within the data set). We tried smaller values of δt in the first set of streamline sections that were extracted for ‘‘fractal’’ analysis (see Sec. III C) and no appreciable difference was found for a given velocity interpolation scheme.

We used two velocity interpolation schemes, a linear second-order accurate (in grid spacing) eight-point scheme, and the third-order Taylor series 13-point scheme (TS13) of Yeung and Pope [12]. These were tested against exact spectral interpolation obtained by summing the full Fourier series at points in continuous space between grid nodes. (DNS data are generated on a periodic domain and are represented by a finite Fourier series.) The cost of using the full spectral interpolation for the simulation of a large number of streamlines is unacceptably large; hence the use of numerically cheaper interpolation schemes, the accuracy of which we test against the exact interpolation (see Sec. IV). We used the

linear and TS13 interpolation schemes to *locate* accumulating streamlines, while TS13 and the full Fourier summation were used to accurately track streamlines in these regions. These accurate streamlines were then subjected to fractal analysis.

Yeung and Pope [12] compared the accuracies of ten interpolation schemes, including the linear and TS13 schemes, on a 32^3 velocity field grid data expressed as a finite Fourier series with no time dependence (frozen field), random phases, and an energy spectrum $E(k) = k^{-5/3} \exp[-3.675(k\eta)^{4/3}]$. They computed errors in fluid particle displacement, and found that TS13 is very accurate, performing better than all other schemes except splines and full spectral interpolation. Specifically, for TS13 in the case where the largest wave number k_{\max} is such that $k_{\max}\eta = 1$, they report an average particle displacement error over many particles that remains smaller than 1% for nearly two integral time scales. For TS13 in the case where $k_{\max}\eta = 4$, they report an average particle displacement error that remains below 0.01% over more than one integral time scale, for a variety of Courant numbers below 0.3. Furthermore, they do not observe an increase in accuracy as the Courant number decreases, but they do observe a fairly dramatic increase in accuracy as $k_{\max}\eta$ increases.

Yeung and Pope [12] find that a suitable criterion for good TS13 particle tracking accuracy is $k_{\max}\eta \geq 1$. As indicated in Table I, in F128 and S128 $k_{\max}\eta \approx 1.6$, whereas $k_{\max}\eta$ is approximately 3.2 in S256 and 6.38 in S512. Balachandar and Maxey [13] demonstrate on specific examples including TS13 that the error with which an interpolation scheme determines the Fourier coefficients of a velocity field increases with wave number. Therefore interpolation errors are smaller for velocity fields with steeper energy spectra. Here the energy spectra decrease at a rate much faster than $k^{-5/3}$.

As an additional test, we computed streamlines around simulated Burgers vortices with characteristics similar to the vortices found in the unforced DNS turbulence of Yeung and Brasseur [11], and found no significant error.

C. Systematic ‘‘fractal’’ analysis of turbulent streamlines

(i) Because we search for streamlines with spiral or accumulating structure, we require an algorithm which can first detect streamline sections with persistently strong curvature (what we call ‘‘persistence of strong curvature’’). The streamline sections that we seek to discard are ‘‘meandering’’ or nearly straight; their curvature changes orientation ‘‘too often’’ along the streamline’s arc length, or is simply too gentle.

This qualitative requirement for persistent curvature is quantified as follows: we first calculate the scalar product of the normal \mathbf{n} to a streamline at two consecutive values of t in the numerical solution of (3.1), i.e., $\mathbf{n}(t) \cdot \mathbf{n}(t + \delta t)$ for all t , and plot this product against the arc length s (as shown in Fig. 3 by the dotted line). If the streamlines were in a 2D plane, $\mathbf{n}(t) \cdot \mathbf{n}(t + \delta t)$ would change value abruptly from 1 to -1 and back to 1 again at those points s on the streamline where the curvature changes sign (inflection points). In 3D space, more complex changes in curvature can occur and we define a somewhat arbitrary threshold to identify spikes in

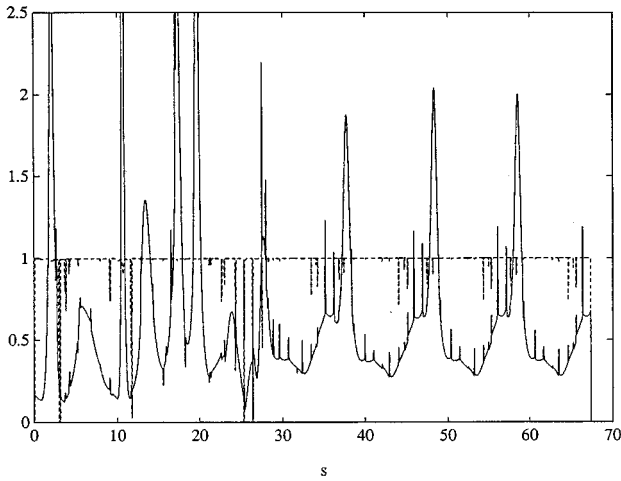


FIG. 3. Curvature $C(s)$ (solid line) and scalar product $\mathbf{n}(t) \cdot \mathbf{n}(t + \delta t)$ (dotted line) against arc length s for one streamline, where $\mathbf{n}(t)$ is the unit normal vector to the streamline at pseudotime t .

$\mathbf{n}(t) \cdot \mathbf{n}(t + \delta t)$. Where the value of $\mathbf{n}(t) \cdot \mathbf{n}(t + \delta t)$ is below that threshold the algorithm automatically decides that there is no ‘‘curvature persistence’’ on the respective segment of streamline. Abrupt jumps in $\mathbf{n}(t) \cdot \mathbf{n}(t + \delta t)$ can be seen in Fig. 3.

The identification of jumps in $\mathbf{n}(t) \cdot \mathbf{n}(t + \delta t)$ is not sufficient for a criterion for ‘‘persistence of strong curvature.’’ We also need a criterion for consistently strong curvature. To quantify strong curvature, the algorithm first identifies a range of arc lengths s where $\mathbf{n}(t) \cdot \mathbf{n}(t + \delta t)$ is consistently larger than a certain value [e.g., in Fig. 3, $\mathbf{n}(t) \cdot \mathbf{n}(t + \delta t)$ is larger than 0.7 from $s=27$ to 67], and then calculates the integral $\int C(s)ds$ of the streamline curvature $C(s)$ over that range of arc lengths s . If $\int C(s)ds$ is larger than a certain value, then, on average, the curvature remains large over the relevant range of arc lengths, and the algorithm isolates that portion of streamline as having a persistence of strong curvature [e.g., in Fig. 3 $\int C(s)ds$ is larger than 2π from $s=27$ to 67 , where $C(s)$ is given by the solid line]. The box-counting algorithm to determine the Kolmogorov capacity is then applied to the streamline segments identified by the algorithm as having persistently strong curvature.

After some experimentation, we chose different threshold values for the linear and TS13 interpolation schemes. For linear interpolation, the thresholds were $\mathbf{n}(t) \cdot \mathbf{n}(t + \delta t) \geq 0.95$ and $\int C(s)ds \geq 3\pi$. TS13 interpolation with the same threshold of 0.95 missed many persistently strongly curved streamlines, either completely or only partially. Consequently, for TS13 we chose $\mathbf{n}(t) \cdot \mathbf{n}(t + \delta t) \geq 0.7$ and $\int C(s)ds \geq 3\pi$. Note that in certain circumstances, $\int C(s)ds$ may be interpreted as a total angle.

This algorithm is still imperfect and may miss some spiral streamlines, but as we report in Sec. IV, the majority of the streamline sections that it did isolate had a well-defined spiral or accumulating character.

(ii) The box-counting algorithm is a central tool of fractal analysis. The approach is to cover a streamline with boxes of size δ and to count the number $N(\delta)$ of boxes that are needed for the covering (see Mandelbrot [14]). In practice, at least three different ranges of length scales must exist in the

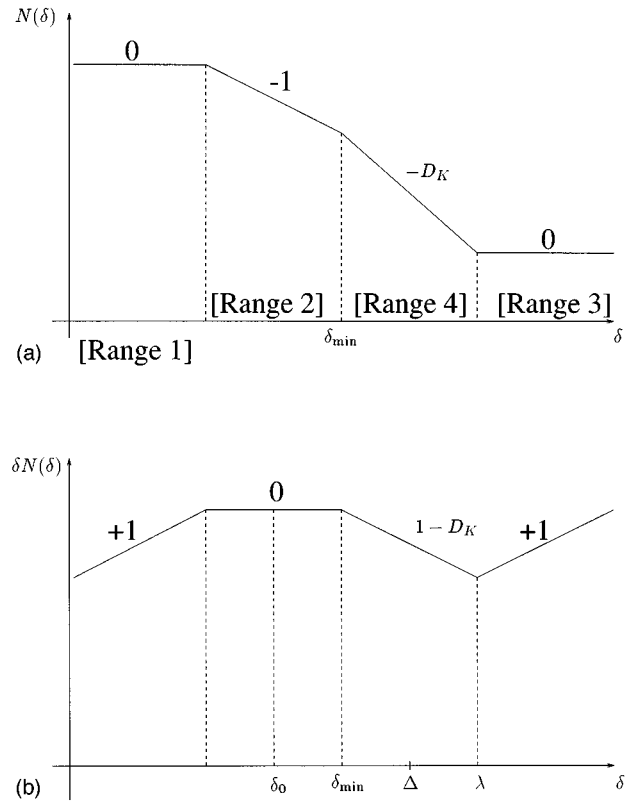


FIG. 4. (a) The box-counting ranges 1–4 shown on a log-log plot of $N(\delta)$ against box size δ . (b) The box-counting ranges 1–4 shown on a log-log plot of $\delta N(\delta)$ against box size δ . The maximum value of $\delta N(\delta)$ before Δ on this plot corresponds to δ_0 . Δ is chosen between ranges 2 and 3.

practical application of box counting, as illustrated in Fig. 4.

Range 1: Because numerically computed streamlines are in fact a sequence of points, if δ is so small that the points of the streamline are resolved, then $N(\delta)$ is a constant equal to the number of points that make up the streamline.

Range 2: As δ increases, a range of length scales δ is reached where the box covering does not resolve the individual points, but sees a smooth one-dimensional object. In that range, $N(\delta) \sim \delta^{-1}$.

Range 3: Finally, when δ is large enough to compare with the extent of the streamline itself, then $N(\delta)$ is again constant and of order 1.

If the streamline has a nonintegral Kolmogorov capacity D_K , then a fourth (‘‘fractal’’) range of length scales δ exists between ranges 2 and 3 in Fig. 4, where $N(\delta) \sim \delta^{-D_K}$ with $D_K > 1$. We seek an algorithm that can detect this fractal range, if it exists, determine its extent, and then measure D_K with suitable confidence. We now describe such an algorithm.

In general,

$$D_K(\delta) = - \frac{\ln[N(\delta)/N_{\min}]}{\ln(\delta/\delta_{\min})}, \quad (3.2)$$

where $N_{\min} \equiv N(\delta_{\min})$ and δ_{\min} is the lower bound of the fractal range. If a fractal range exists with a well-defined value of D_K , then $D_K(\delta)$ is constant (independent of δ) in that fractal range, and $D_K(\delta) = D_K$.

We first choose a scale Δ which, on phenomenological grounds, should be larger than δ_{\min} , but not in range 3. To identify range 4 and specifically find δ_{\min} , the algorithm first looks for the maximum of $\delta N(\delta)$ in the range of length scales bounded by Δ from above [see Fig. 4(b)]. Let us call δ_0 the value of δ where this maximum occurs. The role of the upper bound Δ is to ensure that δ_0 is within range 2 where $N(\delta) \sim \delta^{-1}$, and not within range 4. Thus $\delta_0 \leq \delta_{\min}$.

Then, for successive values of a δ' between δ_0 and Δ ($\Delta > \delta_0$), the algorithm calculates the average value $\bar{D}_K(\delta')$ and the variance $\sigma^2(\delta')$ of

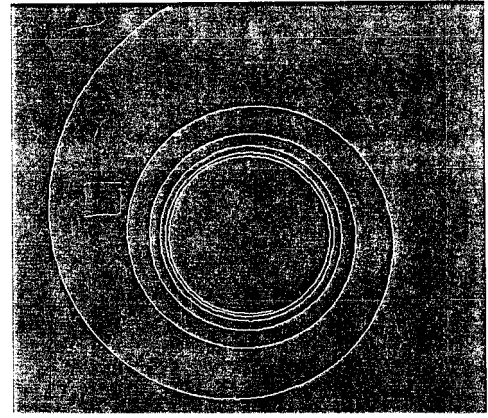
$$D_K(\delta, \delta') = - \frac{\ln[N(\delta)/N(\delta')]}{\ln(\delta/\delta')}, \quad (3.3)$$

over a range of length scales δ that is bounded by δ' from below, and by the Taylor microscale λ from above. The Taylor microscale may be roughly interpreted as being an average radius of the turbulent streamlines (since $\lambda^2 \propto \langle \mathbf{u}^2 \rangle / \langle \omega^2 \rangle$). Whereas in this work the upper bound to range 4 is fixed at λ , in forthcoming work we shall vary the upper bound. Results presented in Sec. IV concerning extremely fine features at the very smaller scales of high vorticity regions indicate that this modification may be necessary. However, it is not necessary for the study of most spiral streamlines in the flow, as shown by the results in Sec. IV.

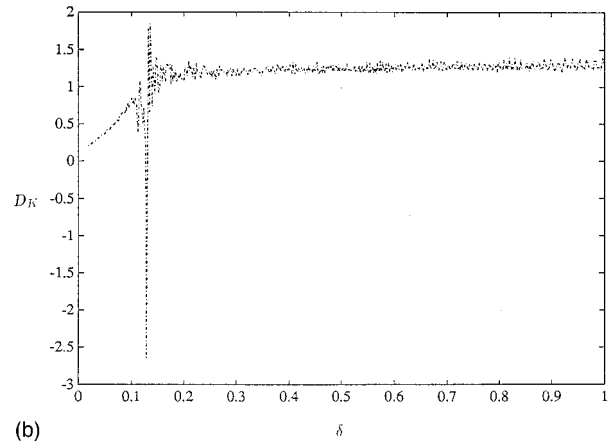
If a fractal range exists with $D_K > 1$, $\sigma^2(\delta')$ decreases with increasing $\delta' > \delta_0$ until δ' reaches the upper bound of range 2 where $\delta' = \delta_{\min}$ (see Fig. 4). Then, as δ' grows beyond δ_{\min} , $\sigma^2(\delta')$ increases because a decreasing sample of values of $D_K(\delta, \delta')$ is used to calculate $\sigma^2(\delta')$, and the function $D_K(\delta, \delta')$ becomes noisier as δ approaches range 4. The lower bound δ_{\min} of the fractal scaling range is the value of δ' where $\sigma^2(\delta')$ is minimized. The measured value of D_K is $\bar{D}_K(\delta_{\min})$.

To illustrate the application of this algorithm, consider the example of the plane spiral $r(\phi) \sim \phi^{-1/2}$ [Fig. 5(a)] which was generated on the computer; r is the distance to the center of the spiral and the angle ϕ is given by $2\pi n_t$ where n_t is a real number between 0 and infinity representing a number of turns. The Kolmogorov capacity of this spiral is $D_K = \frac{4}{3}$ (see Vassilicos and Hunt [4]). Figure 5(b) shows the outcome of the box-counting algorithm on that spiral where the upper bound scale is set equal to 1, the size of the grid spacing in Fig. 5(a). The algorithm identified $\delta_{\min} = 0.127$ to be the minimum scale of the fractal scaling range 4 where it measured $D_K = 1.3$ with accuracy $\sigma^2 = 0.007$. The slight underestimation of D_K is caused by the left-hand side of the $D_K(\delta)$ curve in Fig. 5(b), and can be corrected. We tested our algorithm on a variety of examples of spirals, and found that it works well, although always slightly underestimating the value of D_K .

We remedy this underestimation by generating the mirror image of the curve $D_K(\delta)$ with respect to a horizontal mirror line in the graph (D_K, δ) , and then summing the original and mirror curves together. By varying the vertical coordinate of the mirror line, we find the location of that mirror line that minimizes the standard deviation of the sum of the two curves. That vertical coordinate is the value of D_K that we seek, and in the case of Fig. 5(a), for example, this improved box-counting algorithm yields a $D_K = 1.33$.



(a)



(b)

FIG. 5. (a) Plane spiral $r \sim \phi^{-0.5}$ generated on the computer for the purpose of testing our box-counting algorithm. The location of a point on the spiral is given by the radial coordinate r and the angle $\phi = 2\pi n_t$, where n_t is a real number between 0 and infinity that represents the number of turns of the spiral. (b) Result of box counting on the plane spiral of Fig. 5(a). Kolmogorov capacity $D_K(\delta)$ versus box scale δ . The algorithm measured $D_K = 1.3$ with $\sigma^2 = 0.007$ and accurately located δ_{\min} between 0.1 and 0.2.

IV. DESCRIPTION OF THE PROCEDURE AND RESULTS

A. Analysis of 128^3 data

Most studies of small-scale turbulence structure focus on subjective and visual descriptions of flow structure without quantified measures of flow topology and geometry and no statistics of such measures either. The Kolmogorov capacity is such a measure. D_K is a direct measure of nontrivial accumulations of length scales on a streamline, providing a local nonstatistical quantification of a geometrical cascade of length scales of motion.

To acquire statistics of different such local ‘‘cascades’’ of length scales within the turbulence, we calculated approximately 4000 streamlines on each 128^3 grid of the F128 and S128 data sets, beginning from points spaced uniformly eight grid nodes apart from one another. These streamlines were calculated by solving (3.1) in the instantaneous velocity field, up to pseudotime $t = 10T_E$, where T_E is the Eulerian integral time scale of the turbulence.

After integration of all 4000 streamlines in both data sets, we searched for ‘‘persistence of strong curvature’’ using the

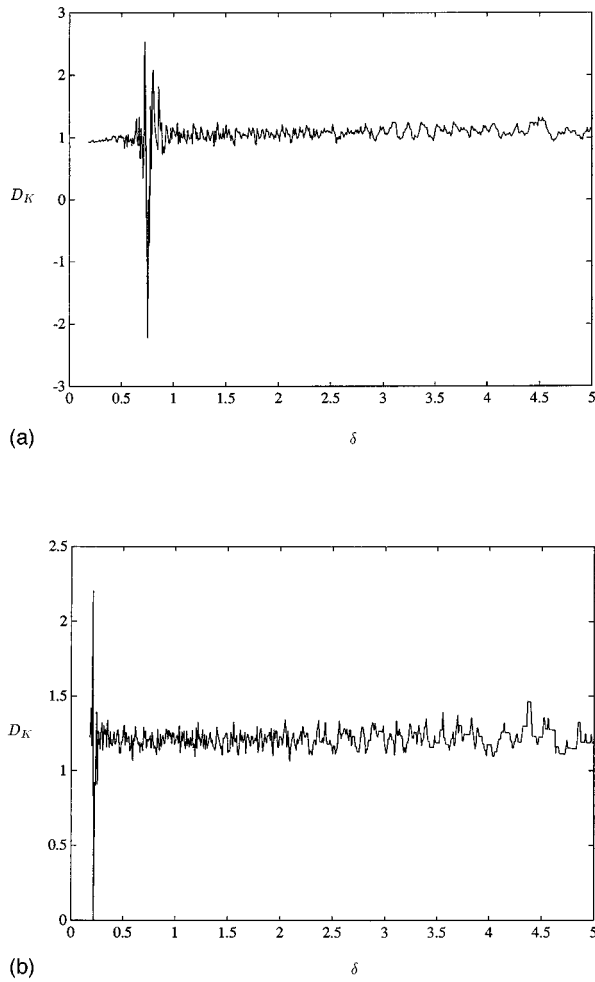
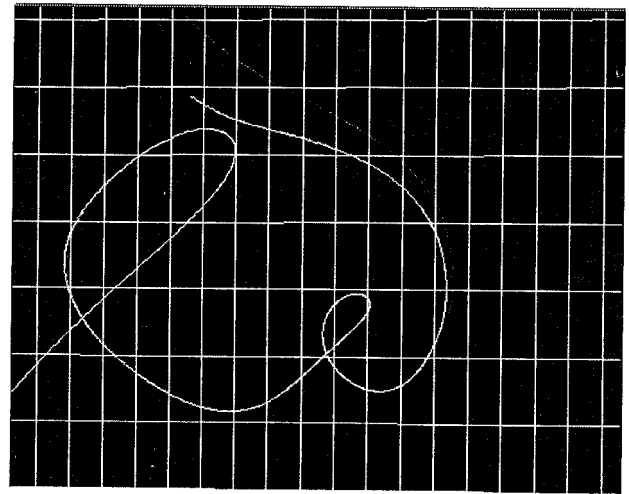


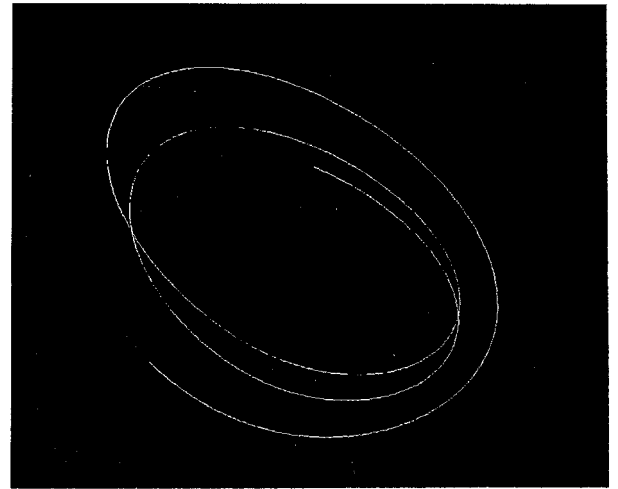
FIG. 6. Examples of box-counting results for two spiral streamlines in the DNS turbulence. The Taylor microscale $\lambda \approx 5$. The Kolmogorov scale $\eta \approx 0.55$. Both D_K and δ_{\min} are clearly obtained by the algorithm. (a) $D_K \approx 1.05$ and $\delta_{\min} \approx 0.75 \approx 1.4\eta$, (b) $D_K \approx 1.25$ and $\delta_{\min} \approx 0.2 \approx 0.36\eta$.

algorithm described in the preceding section. 783 streamline sections in F128 and 795 streamline sections in S128, one out of five computed streamlines, had persistently strong curvature. This is a large number considering that only one streamline was computed in each realization of the large scales, i.e., the initial points of the computed streamlines were nearly one integral length scale L_p apart from each other ($L_p \approx 11\Delta x$ in F128 and $L_p \approx 12.4\Delta x$ in S128). Using a high-quality graphics workstation, we visualized all streamline sections with persistent strong curvature, and of these 386 in F128 and 380 in S128 clearly had an accumulating geometry and 172 in F128 and 180 in S128 lay on *different* vortex tubes. The statistics of Kolmogorov capacities of streamlines are obtained from this subset of 172 and 180 independent streamline sections.

Figure 6 shows two examples of box-counting results for two of the 172 and 180 streamlines just mentioned. In both cases a very well-defined scaling is found over a range of scales from near the Kolmogorov scale η to the Taylor microscale $\lambda \approx 5\Delta x$. The box-counting algorithm works well and provides both D_K and δ_{\min} accurately. Note that the smallest length scale δ_{\min} of the range of self-similar box-



(a)



(b)

FIG. 7. (a) TS13 interpolation of a spiral streamline in the DNS turbulence (the faintest of the two curves) compared with interpolation by full Fourier summation of the same streamline. For the TS13 interpolation, we measured $D_K \approx 1.1$. (b) Another spiral streamline where $D_K \approx 1.33$. Here the TS13 and Fourier interpolations are identical.

counting scaling is slightly smaller than η for one streamline and slightly larger for the other. There is also a variation of D_K from streamline to streamline. In Fig. 6(a), for example, $D_K \approx 1.05$, and in Fig. 6(b) $D_K \approx 1.25$. Figures 6(a) and 6(b) were not chosen because they are our best results. The good quality of the self-similar scalings detected on these streamlines in a range of length scales from about η to λ is typical of the 783 and 795 streamline sections that were singled out by the algorithm for the detection of persistence of strong curvature.

We tested the accuracy of TS13 interpolation against the full Fourier summation (“exact” interpolation) for 15 of the 783 streamline sections that form our conditional statistical sample from the F128 data set. (The prohibitively high computational cost involved prevented the use of Fourier summation on all streamline segments.) Figure 7 shows two typi-

cal comparisons. In Fig. 7(a) the TS13 interpolation diverges after some time from the “exact” interpolation obtained by full Fourier summation. In Fig. 7(b) the agreement is excellent over the entire streamline section. The Kolmogorov capacity D_K of the streamline section in Fig. 7(b) is appreciably larger than the D_K of the streamline section in Fig. 7(a). This is typical of what we observed in the 15 tests; interpolation errors are larger when the D_K is smaller. Furthermore, the D_K measured for streamlines using TS13 interpolation usually *underestimate* the true value of D_K . This is easily understood; interpolation errors come from missing steep bends, as in Fig. 7(a) where the TS13 interpolation (the faintest curve on the plot) misses the curvature of the “exact” interpolation, and therefore produces a spiral or accumulating pattern which is less space filling than it should be, thus leading to an underestimation of D_K (see Vassilicos and Hunt [4] for a discussion of the “space fillingness” of spirals). The bends of streamlines are generally steeper the closer the value of D_K is to 1. Consequently, if a measure of D_K greater than 1 using TS13 interpolation is in error, the error is an underestimate in D_K and D_K is indeed greater than 1. The accuracy of measured D_K improves with increasing $D_K > 1$ and the interpolation seems to increasingly underestimate D_K as $D_K \rightarrow 1$. Note from Figs. 7(a) and 7(b) that a surprisingly small number of turns is needed to detect the Kolmogorov capacities.

In Fig. 8 we plot two histograms of measured D_K for the 172 and 180 independent streamline sections that have a persistence of strong curvature in F128 and S128, respectively. Of these streamline sections, 39% in F128 and 47% in S128 have $D_K > 1$, specifically D_K between 1 and 1.5 in F128 and between 1 and 1.6 in S128 (Table II). Figure 9 shows an example of a scatter plot of D_K versus the minimum length scale δ_{\min} in the range where the corresponding D_K are well defined. Note the concentration of values of δ_{\min} around Δx and around $\Delta x/4$. A typical example of a scatter plot of D_K versus σ^2 is given in Fig. 10, where σ^2 is the variance of $D_K(\delta)$ about D_K (see Sec. III C). In many cases (often when D_K is large) D_K is well defined (i.e., σ is very small compared to D_K) from λ to δ_{\min} . In particular, $D_K - \sigma > 1$ in approximately one-fifth of the cases considered (32 out of 172 in F128 and 34 out of 180 in S128). These results are obtained from simulations where $\lambda \approx 5\Delta x$ and $\Delta x \approx 1.8\eta$, and the values of δ_{\min} cluster around Δx and $\Delta x/4$.

B. Analysis of 256³ and 512³ data

To show that the identification of a significant number of streamlines with $D_K > 1$ and that the values of δ_{\min} obtained from the 128³ data are not artifacts of the finite grid resolution, we repeated the same calculations with the data sets S256 and S512, where $\lambda/9.8 \approx \Delta x \approx 0.92\eta$ and $\lambda/19.4 \approx \Delta x \approx 0.46\eta$, respectively. We calculated approximately 2000 and 1000 streamlines, respectively, on the 128³ grids of the S256 and S512 data sets by solving (3.1) in the instantaneous velocity field up to pseudotime $t = 10T_E$. The number of streamline sections found with persistently strong curvature is 560 in S256 and 173 in S512, that is, respectively, one out of 3.5 and one out of 5.8 computed streamlines, which compares reasonably well with the results from F128 and S128. Visualizing all streamline sections with persistently strong

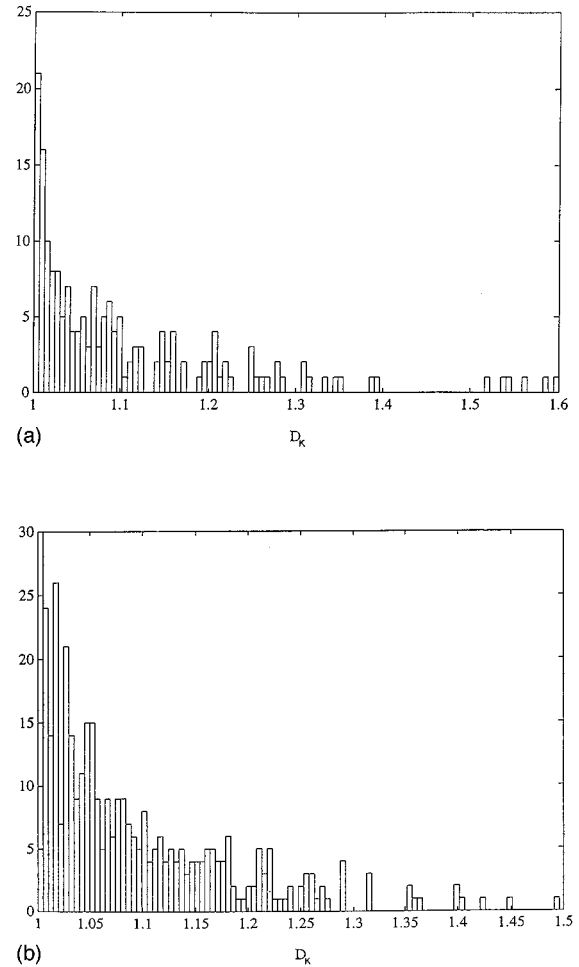


FIG. 8. Histograms of D_K including only $D_K > 1$ (a) for the 172 independent streamline sections detected by the algorithm for persistence of strong curvature in F128 and (b) for the 180 independent streamline sections detected by the algorithm for persistence of strong curvature in S128 (“independent” implies that each streamline coils around a different vortex tube).

curvature, it turned out that of these, respectively, 285 and 130 clearly have an accumulating geometry, and 98 and 31 lie on different vortex tubes in the S256 and S512 high-resolution velocity fields. Of these independent streamlines, 34% have a D_K strictly larger than 1 and not larger than 1.47 in S256 and 24% have a D_K strictly larger than 1 and not larger than 1.26 in S512.

It must be stressed that both S256 and S512 are highly resolved *subsets* of the original S128 velocity field, corresponding to a 64^3 and a 32^3 corner of S128 ($\frac{1}{8}$ and $\frac{1}{64}$ of the computational domain). We checked that, among the streamlines calculated only in those corners of S128 that correspond to S256 and S512, the percentages of independent streamlines with an accumulating geometry that have a D_K strictly larger than 1 are 30% and 18%, respectively, which compare well with (and are in fact smaller than) the percentages obtained from S256 and S512 (Table II). Furthermore, the largest values of D_K measured in the corners of S128 that correspond to S256 and S512 are 1.48 and 1.26, respectively. Hence the percentages of independent accumulating streamlines with $D_K > 1$ increase and the maximum values of D_K are unchanged when the resolution is improved.

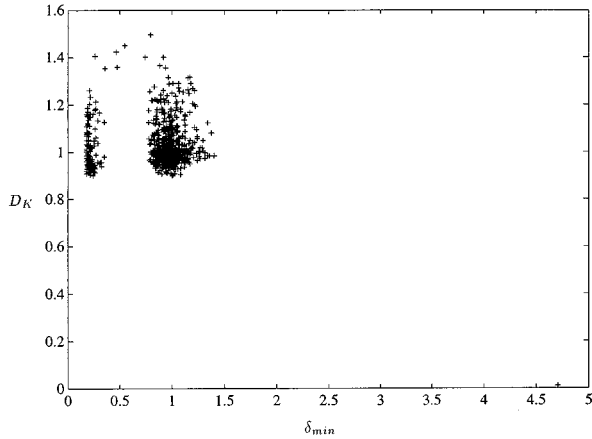


FIG. 9. Scatter plot of D_K against δ_{\min} for the 172 independent streamline sections extracted from F128. The units on the abscissa are such that $\Delta x = 1 = 1.8\eta$. The apparent sharp cutoff in data points at about 0.2 is an artifact of having artificially restricted the search for δ_{\min} to values larger than approximately 0.3η in the algorithm described in Sec. III C (ii).

Scatter plots of D_K versus δ_{\min} for the high-resolution data sets S256 and S512 give results similar to Fig. 10. It is striking that the values of δ_{\min} cluster around 2η and $\eta/2$ in all data sets F128, S128, S256, and S512 independently of the grid resolution. In Fig. 11 we plot histograms of σ^2 showing that the Kolmogorov capacities are increasingly well defined with increasing resolution (σ^2 decreases on average from S128 to S256 to S512).

From visualizations such as Fig. 12 and 13, we observe two very different types of accumulation of length scales on the streamlines that have a persistence of strong curvature. In Fig. 12 the streamlines accumulate towards a central axis and the accumulation is primarily radial, whereas in Fig. 13 the streamlines accumulate towards a limit circle and the accumulation of length scales is *along* the vortex tube. The limit circle lies in a region of the vortex tube where the magnitude of the vorticity attains a local minimum (see Fig. 13). These two types of streamline accumulating topology appear to be quite generic in the small-scale turbulence field that we have studied, and cannot be both accounted for in terms of the simple straining fields of the Burgers and the Lundgren vortices. Furthermore, as we discussed in Sec. II B, the very existence of persistently curved streamlines with well-defined $D_K > 1$ at the low Reynolds numbers of the present simulations is evidence that the vortex tubes where these streamlines reside are not Burgers vortices.

C. Streamlines of the most intense vortices

In the results of Secs. IV A and IV B, accumulating geometry was extracted from streamlines initiated from arbi-

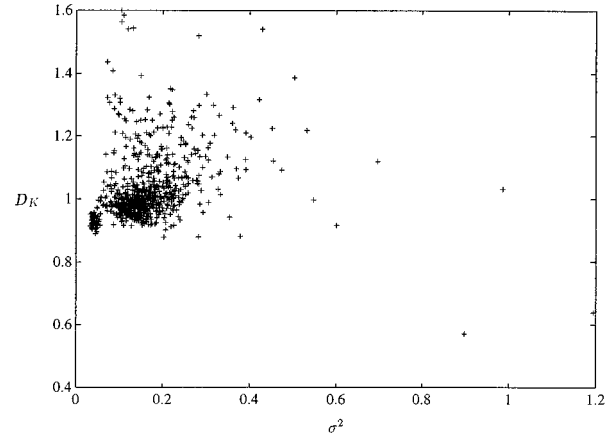


FIG. 10. Scatter plot of D_K against σ^2 , the variance of $D_K(\delta)$ about D_K , for the 180 independent streamline sections extracted from S128.

trarily placed points uniformly spaced over subregions of the data sets. The many visualizations that were made of the spiral trajectories relative to the local enstrophy field strongly suggest that the streamlines with $D_K > 1$ are primarily associated with the more intense vortex tube structures. We expect, therefore, that a larger number of independent streamlines with persistently strong curvature would be found if the extraction of streamlines were to begin within those data points with the highest relative vorticity. We also want to check that a similar if not higher percentage of independent persistently curved streamlines from this specially chosen set have $D_K > 1$.

We integrated streamlines beginning from all points in the F128 data set with the highest relative value of enstrophy such that these points covered 1% of the entire data set. Although Jiménez *et al.* [7] described these points as defining the most intense vortex tubes (“worms”), not all the chosen points are within well-defined tubelike concentrations of vorticity, and we therefore expect only a fraction to display “persistent curvature.” Furthermore, of those streamlines that do display persistent curvature, several may surround the same vortex tube; thus only a fraction of the total will define independent streamlines surrounding different vortex tube elements.

We integrated approximately 23 000 streamlines where the enstrophy ω^2 is larger than 6.3 times the rms of the enstrophy throughout the field of the simulation. The totality of these intense vortex tubes is shown in Fig. 14. The streamlines were integrated for five integral time scales T_E using the TS13 interpolation scheme. The algorithm for the detection of persistence of strong curvature detected such a streamline section in approximately one of every four streamlines integrated. Of these, 1425 were independent (i.e.,

TABLE II. Highlights of analyses of streamline geometry.

	F128	S128	S128	S256	S256	S512	F128
Portion of box extracted	all	all	1/8	1/8	1/64	1/64	all
No. of streamlines extracted	4000	4000	500	2000	62	1000	22 987
% independent streamlines, $D_K > 1$	39%	47%	30%	34%	18%	24%	42%
Maximum D_K	1.5	1.6	1.48	1.47	1.26	1.26	1.68

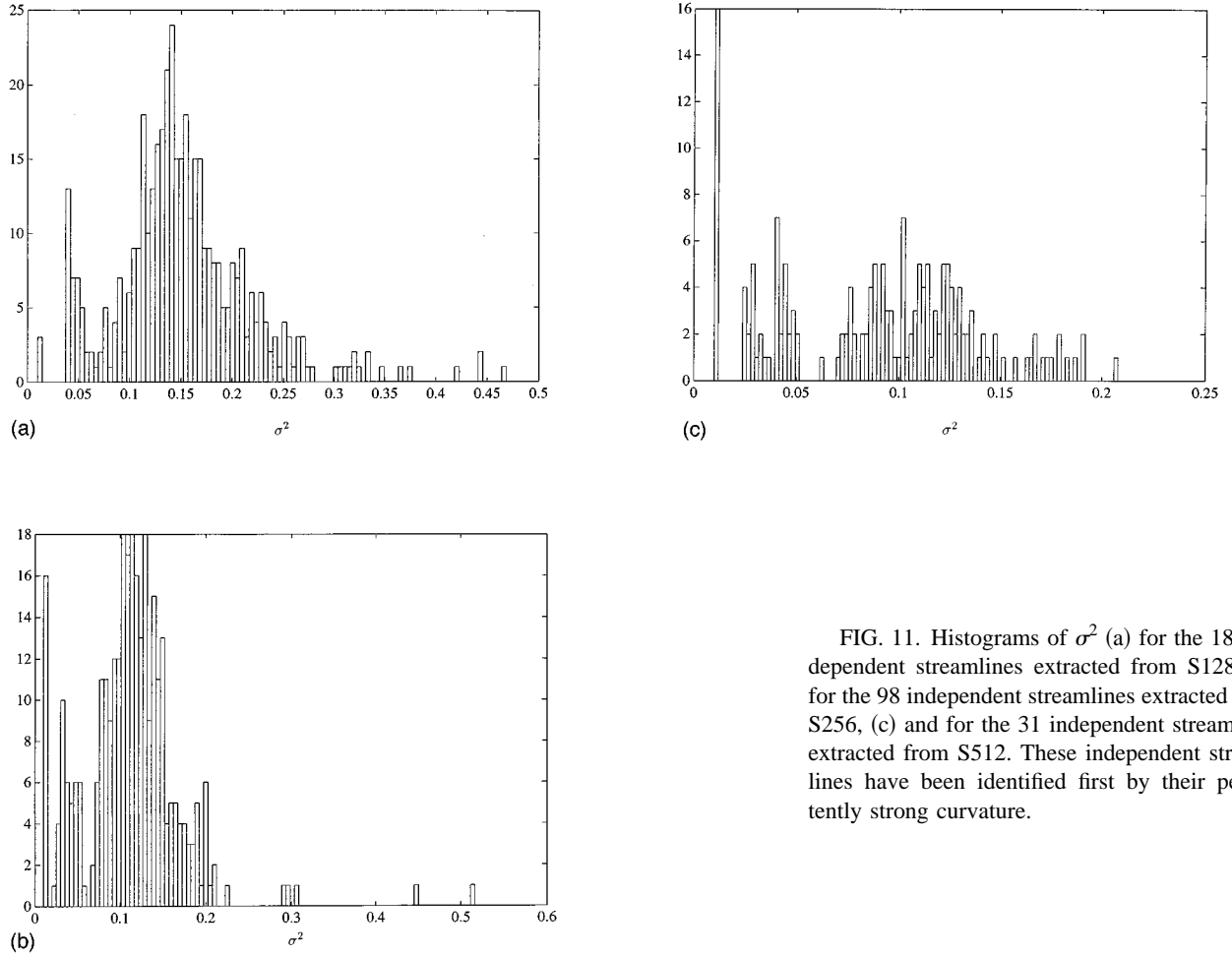


FIG. 11. Histograms of σ^2 (a) for the 180 independent streamlines extracted from S128, (b) for the 98 independent streamlines extracted from S256, (c) and for the 31 independent streamlines extracted from S512. These independent streamlines have been identified first by their persistently strong curvature.

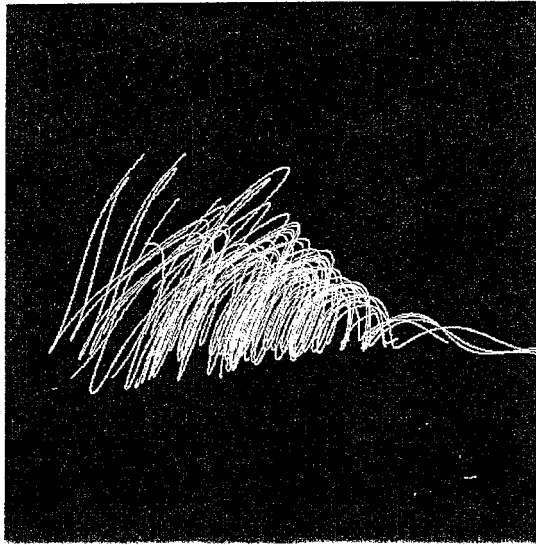
on different vortex tubes) persistently curved streamlines. This number is much higher than the number of streamlines extracted using an arbitrary uniform placement of initial points.

Figure 15 is a histogram of the values of D_K for the 1425 independent streamline sections in the most intense vortex tubes (those which occupy only 1% of the total domain). Each one of these 1425 nonoverlapping streamlines was chosen *at random* among approximately one to five streamlines detected on the *same vortex tube*. We used precisely the same box-counting algorithm to determine D_K as in Sec. IV A, in particular with the upper bound cutoff scale still equal to λ . The values of D_K below 1 suggest that λ is too large an upper bound for the self-similar range of the geometry of the streamlines at these extremely small scales of motion. Clearly though, a large number of streamlines were found with accumulating geometry and $D_K > 1$, specifically 42% of the 1425, which is a similar percentage to the one found with randomly placed streamlines in the F128 and S128 data sets. In fact, more accumulating streamlines with $D_K > 1$ were extracted than what is shown in Fig. 15, since we chose a representative streamline for each vortex tube rather than pick out the streamline with the largest and best defined D_K . The streamlines with $D_K > 1$ are well defined over a range of length scales extending from λ to δ_{\min} . We also found that, at these very small scales, δ_{\min} is often approximately equal to $\eta/2$. Following the discussion in Sec.

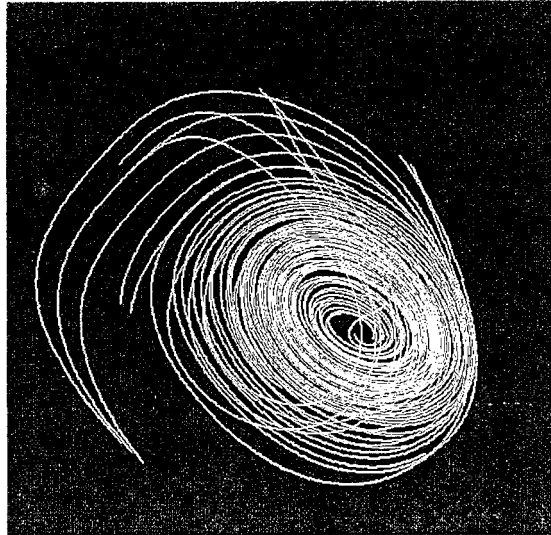
II, the nonintegral values of D_K that we observe on spiral-helical streamlines may reflect localized near-singular flow structures in the regions surrounded by these streamlines. These local near singularities may extend over a significantly wide range of scales bounded from below by a *local* viscous cutoff scale that is a function of the local flow structure, and may therefore differ from one near-singular vortex tube to another. In the following subsection we study whether the vorticity profile across vortex tubes can be approximated by a well-resolved Gaussian at the resolution of this paper's DNS turbulence, in which case the width of this Gaussian could provide a measure of the local viscous cutoff scale of the vortex tube.

D. The vorticity profile across the vortex tubes

As discussed in Sec. II, the existence of streamlines with $D_K > 1$ in such a low Reynolds number turbulence indicates that these vortex tubes are not Burgers vortex tubes. The analysis presented in this subsection shows that, even in the highly resolved S512 turbulent velocity field, the vorticity profile across the width of some of the vortex tubes is not a well-resolved Gaussian (by which we mean that it is not well resolved, or non-Gaussian, or both). This analysis is based on the spatial correlation of the enstrophy $\omega^2 = \boldsymbol{\omega} \cdot \boldsymbol{\omega}$ with the square of the viscous force $f^2 = \mathbf{f} \cdot \mathbf{f}$ ($\mathbf{f} = -\nu \rho \nabla \times \boldsymbol{\omega}$) in the vortex tubes around which streamlines with persistent curvature are identified. This correlation is



(a)



(b)

FIG. 12. From the DNS isotropic turbulence with $Re_\lambda \approx 21$. (a) Projection of vortex tube streamlines on a plane transversal to the vortex tube in the small-scale turbulence. (b) Projection of the same streamlines on the azimuthal plane of the vortex tube. The Kolmogorov capacities D_K of these streamlines vary between 1.2 and 1.3.

$$C = \frac{\langle (f^2 - \langle f^2 \rangle)(\omega^2 - \langle \omega^2 \rangle) \rangle}{\langle (f^2 - \langle f^2 \rangle)^2 \rangle^{1/2} \langle (\omega^2 - \langle \omega^2 \rangle)^2 \rangle^{1/2}}, \quad (4.1)$$

where the brackets $\langle \rangle$ imply conditional averages over grid boxes visited by streamline segments with persistent curvature and over those *neighboring* grid boxes with *larger* values of enstrophy. No more grid boxes are included in the conditional average once no other neighboring grid boxes can be found with larger enstrophy. In this way local volumes of concentrated enstrophy equal to and larger than the enstrophy along a persistently curved streamline section are extracted from the data set for analysis. The averages in (4.1) are carried out over these individual volumes of high enstrophy (the vortex tubes) where the streamline sections coil.

We calculate the average \bar{C} of C over many vortex tubes extracted in the manner just described, and to probe increasingly small scales of vortex motion we calculate \bar{C} over increasingly small percentages of the total volume in these vortex tubes. We do this by averaging over those portions of individual extracted vortex tubes where $\omega^2/\omega_{\max}^2 \geq \omega_{\text{th}}^2/\omega_{\max}^2$ for increasing values of the threshold (ω_{th}^2) relative to the local maximum enstrophy ω_{\max}^2 in each vortex tube. In this way, we obtain curves $\bar{C}(\omega_{\text{th}}^2/\omega_{\max}^2)$ as in Fig. 17.

Due to viscous stresses deep within the vortex core, we may expect the vorticity to reach a constant finite value at the center of the vortex tubes, indicating solid body rotation at the center, as in the case of the Burgers vortex [Fig. 16(a)]. Close to the center the viscous force may therefore decrease to 0. If the vortices are sufficiently well resolved and if local cores of solid body rotation exist and extend over a grid size Δx or more, then C should be negative for large enough values of $\omega_{\text{th}}^2/\omega_{\max}^2$. This is because f^2 should be small in the innermost viscous core where ω^2 is largest, whereas at the edge of the vortex core, where vorticity gradients are highest, the viscous force should reach a maximum [see example of the Burgers vortex, Fig. 16(a)]. Hence, as the threshold ω_{th}^2 is increased and C is calculated over deeper parts of the inner cores of the vortices and over a smaller number of increasingly strong vortices, C should tend to -1 . This is indeed the case for the Burgers vortex where, as shown in Fig. 16(b), C reaches -0.9 when $\omega_{\text{th}}^2/\omega_{\max}^2 \approx 0.2$. Figure 16(b) is an analytical result derived from (2.7) and is purely a consequence of the Gaussian vorticity profile of the Burgers vortex.

What we observe in the simulated turbulence is very different from Fig. 16(b). Figure 17(a) shows that in simulation F128 \bar{C} remains positive over all values of $\omega_{\text{th}}^2/\omega_{\max}^2$, and Fig. 17(b) shows that in simulation S128 \bar{C} decreases slowly to small negative values that are strictly greater than -0.1 . In all the plots of \bar{C} versus $\omega_{\text{th}}^2/\omega_{\max}^2$ (Fig. 17), the part of the curve where $\omega_{\text{th}}^2/\omega_{\max}^2 \geq 0.7$ is insignificant because fewer than eight grid points are sampled above this threshold (grid points are separated only by a distance Δx).

To sample more deeply within the vortex tubes, we repeat the calculation of the curve $\bar{C}(\omega_{\text{th}}^2/\omega_{\max}^2)$ using the high-resolution data sets S256 (where $\Delta x \approx 0.92\eta$) and S512 (where $\Delta x \approx 0.46\eta$). Whereas Fig. 17(b) is obtained from vortex tubes in the entire volume of S128, Fig. 17(c) and 17(d) are obtained from vortex tubes, respectively, in $\frac{1}{8}$ of the total volume of S256 and $\frac{1}{64}$ of the total volume of S512. This is done because of computer limitations so that we always use a 128^3 grid when calculating correlations. Hence the correlation in S128 is calculated over 180 extracted vortex tubes, the correlation in S256 over 98 extracted vortex tubes and the correlation in S512 over 31 extracted vortex tubes (see Secs. IV A and IV B).

Because the sample sizes are different among the three data sets and are not large, especially for the S512 data set, the correlation plots in Figs. 17(b)–17(d) do not overlap. Nevertheless, these correlations do agree in one surprising and important respect: the spatial correlation \bar{C} between the viscous force and the enstrophy in the extracted vortex tubes does not fall below -0.1 for all the thresholds $\omega_{\text{th}}^2/\omega_{\max}^2$ considered, in particular $\omega_{\text{th}}^2/\omega_{\max}^2$ between 0 and 0.3. This ob-

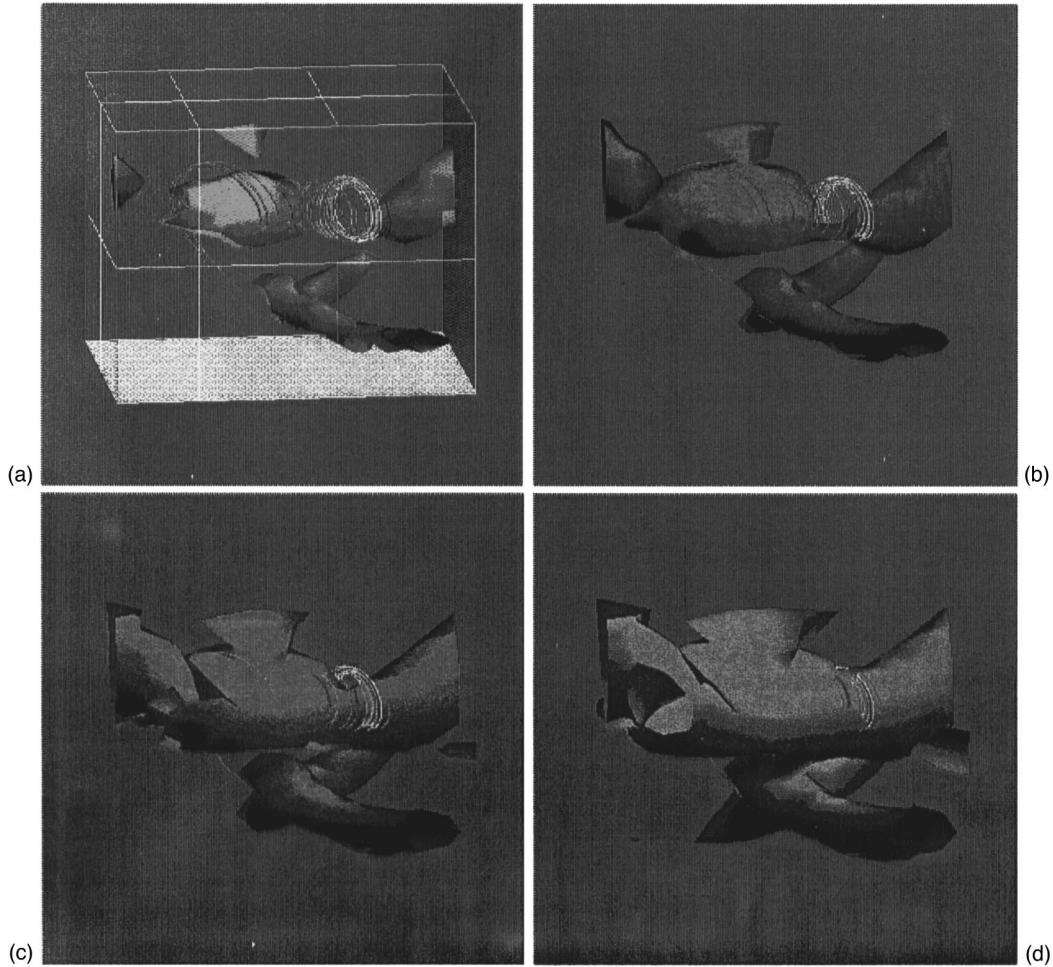


FIG. 13. A number of axially accumulating streamlines with $D_K \approx 1.33$ around a small-scale vortex tube in the DNS isotropic turbulence with $Re_\lambda \approx 19$. The vorticity vectors are directed along the axis around which the streamlines coil, and point from left to right. The axially accumulating streamlines are plotted with isoenstrophy surfaces with ω^2 equal to (a) 15 rms, (b) 12 rms, (c) 10 rms, and (d) 8 rms (the rms of ω^2 is over the entire 128^3 flow simulation). Note that the streamlines approach limit circles at the region of minimum enstrophy along the axis.

servation is independent of whether the grid spacing is roughly double, equal, or half the Kolmogorov length scale η .

These observations are significant because a well-resolved Gaussian vorticity profile across the azimuthal plane of the vortex (as assumed, for example, by Jiménez *et al.* [7]), has, from Fig. 16(b), a correlation between the enstrophy and the square of the viscous force that is below -0.1 for all $\omega_{th}^2/\omega_{max}^2 \geq 0.05$. Figure 17, where $\bar{C} > -0.1$ for $\omega_{th}^2/\omega_{max}^2$ between 0.0 and 0.3, is therefore inconsistent with a well-resolved Gaussian spatial distribution of vorticity across the extracted vortex tubes. Furthermore, if we anticipate the existence of a Gaussian spatial distribution of vorticity very deep inside the core of the vortex where effects of friction dominate, we can then conclude that the flow structure in the vortex tubes extracted by our extraction algorithm is not totally smoothed out by viscosity around scales of order η .

It is interesting to note that if we restrict the sample over which the average value \bar{C} is calculated only to those vortex tubes where we detect streamlines having strong persistent curvature and a well-defined nonintegral D_K , the curves $\bar{C}(\omega_{th}^2/\omega_{max}^2)$ remain qualitatively the same as in Fig. 17.

V. CONCLUSIONS

Self-similar near-singular flow structure can be advantageously identified and characterized by the self-similarity of its streamlines in real space. We prove that the vorticity field in an axisymmetric flow where spiral-helical streamlines have well-defined nonintegral Kolmogorov capacities is necessarily singular at the axis of symmetry, and find spiral-helical streamlines around small-scale vortex tubes of low Reynolds number isotropic and decaying DNS turbulence that have nontrivial scaling properties with well-defined nonintegral Kolmogorov capacities over a fairly long range of length scales extending from around the Kolmogorov length scale to the Taylor microscale. Further studies over a range of Reynolds numbers are needed to establish whether the upper scale of the geometrical self-similar range of streamlines indeed scales with the Taylor microscale. Variations in Reynolds number are also needed to establish the scaling of the streamline cutoff scales δ_{min} , and to verify the existence of two well-defined scales near η . By comparing the spatial correlation between enstrophy and the square of viscous force in DNS vortex tubes to that in vortex tubes with a

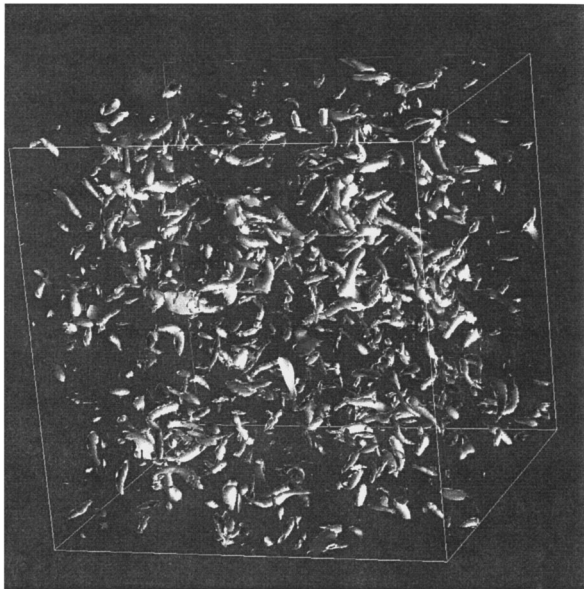


FIG. 14. Enstrophy isosurfaces in the entire 128^3 turbulent flow field (F128) at $\omega^2=6.3$ rms. The vortex tubes shown in this figure cover 1% of the simulation domain, corresponding to the definition of “worms” in Jiménez *et al.* [7].

Gaussian radial distribution of vorticity we conclude that the vorticity profile of some DNS vortex tubes is not a well-resolved Gaussian even when the DNS resolution is exceptionally high by the standards of current simulations (grid size as small as $\Delta x \approx 0.46\eta$).

Some additional clues as to the internal structure of these vortex tubes are obtained from the study of streamlines; we find that the self-similar geometry of streamlines with persistence of strong curvature in low Reynolds number isotropic turbulence has an accumulating cascade of length scales either towards a point on the axis of the vortex (spiral-helical streamlines) or towards a circle in axial regions of low vorticity magnitude. Nonintegral Kolmogorov capacities are found for either type of streamline accumulation. Our findings also suggest that a significant number of vortex tubes in

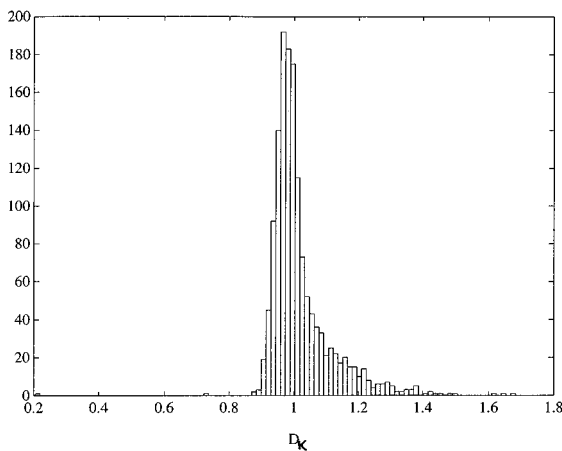
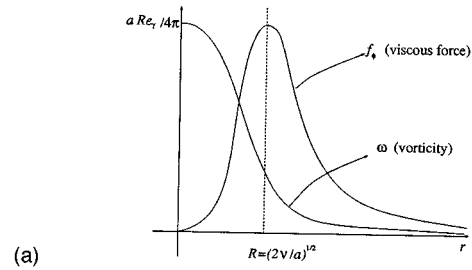
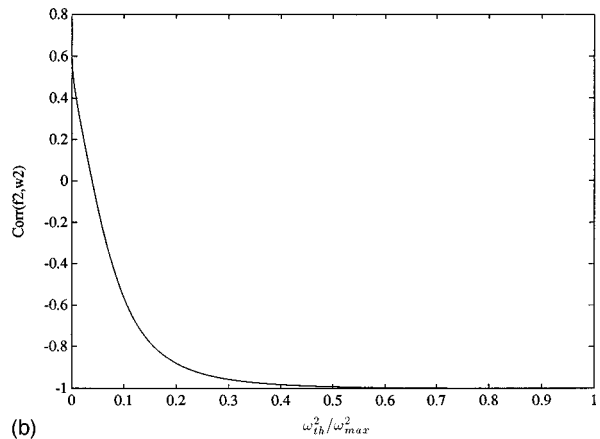


FIG. 15. Histogram of D_K for the 1425 independent streamline sections with persistence of strong curvature in the vortex tubes of Fig. 15.



(a)



(b)

FIG. 16. The Gaussian enstrophy profile of the Burgers vortex and its consequences. (a) Schematic profile of radial variations of enstrophy and the viscous force. For a Burgers vortex, the viscous force per unit volume $\mathbf{f} = -\nu\rho\nabla \times \boldsymbol{\omega}$ (ρ is the density of the fluid) has only one nonzero component which is azimuthal, $f_\phi = -\rho(a^2\text{Re}_\nu/8\pi)re^{-ar^2/4\nu}$. The viscous force is negligible deep within the core and far from the vortex, and rises to a maximum at the outer edge of the vortex core, exactly at $R = \sqrt{2\nu/a}$. At the center of the vortex, where the vorticity is maximum and finite, the viscous force vanishes, indicating solid body rotation at the center. (b) Spatial correlation C , between the square of the viscous force and enstrophy, against $\omega_{th}^2/\omega_{max}^2$ for the Burgers vortex. Exact analytic curve derived from (2.7) and the above equation [itself derived from (2.7)].

low Reynolds number isotropic turbulence are not Burgers vortices.

The Reynolds number is too low in these simulations for the energy spectrum of the small-scale turbulence to exhibit an asymptotic self-similar form. Yet, with the Kolmogorov capacity of streamlines we are able to detect nontrivial self-similar geometry in local regions in the flow, even when the curved streamlines exhibit only a couple turns. This ability to extract self-similar structure with minimal information shows the usefulness of the Kolmogorov capacity of the flow geometry as a localized measure of self-similar scaling and near-singular flow structure that does not require a large range of length scales to detect self-similar flow topology. We have shown that the Kolmogorov capacity of streamlines can provide an effective measure of the internal near-singular structure of vortex tubes and can be used when the resolution and/or the Reynolds number are low.

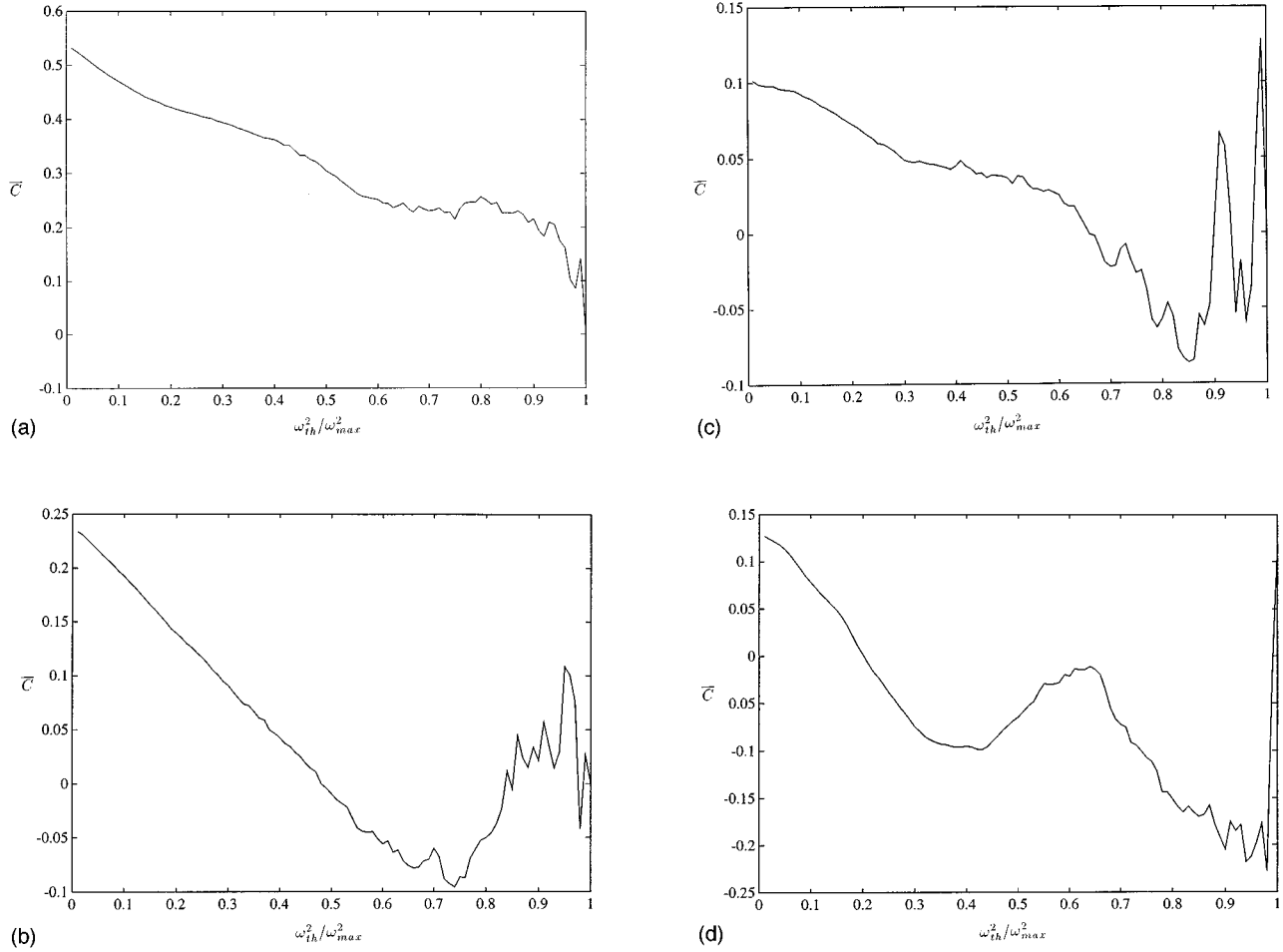


FIG. 17. Ensemble averaged spatial correlation \bar{C} of enstrophy with the square of the viscous force against enstrophy threshold $\omega_{th}^2/\omega_{max}^2$. The ensemble averaging includes only the vortex tubes where streamlines were detected with persistent curvature. (a) F128, (b) S128, (c) S256, and (d) S512.

ACKNOWLEDGMENTS

We are particularly grateful to B. P. Moquin for helping with the writing and running of the postprocessing codes, for the visualizations, and for generating most of the figures in this paper. We are especially grateful also to Lian-Ping Wang for creating data sets S128, S256, and S512 for our use. Support for this work came from British Gas and the Royal Society (J.C.V.), and the Office of Naval Research Grant No. N00014-92-J-1417 (J.G.B.), Air Force Office of Scientific Research Grant No. 90-0113 (J.G.B.), and Army Research Office Grant No. DAAL03-92-G-0117 (J.G.B.) of the United States. Computing time was made available by NAS of NASA–Ames Research Center, U.S.A.

APPENDIX: THE INVISCID LUNDGREN VORTEX: A NEARLY AXISYMMETRIC “COMPLEX” SINGULARITY

The Lundgren vortex is an *asymptotic* solution of the 3D Navier-Stokes equations as time $t \rightarrow \infty$. A particular case of this vortex is a sum of 2D semi-infinite spiral vortex sheets that are subjected to differential rotation and persistent strain in a plane aligned with the vorticity ω . The basic ingredient

of the Lundgren collection of spiral vortex sheets is a single unstrained and inviscid 2D spiral vortex sheet which, in cylindrical coordinates (r, ϕ, z) , is given by

$$\omega(r, \phi, t) = 2\pi f(r) \delta(\phi - \Omega(r)t), \quad (\text{A1})$$

where the vorticity $\omega(r, \phi, t)$ is in the z direction, and δ is the Dirac delta function. Equation (A1) is a long-time asymptotic solution of the Euler equations provided that

$$rf(r) = \frac{d}{dr} r^2 \Omega(r) \quad (\text{A2a})$$

and

$$\frac{d}{dr} \Omega(r) < 0. \quad (\text{A2b})$$

The circulation around a circle of radius r is $\gamma(r) = 2\pi r^2 \Omega(r)$, the ϕ -averaged vorticity is $f(r)$, and (A2a) is simply Kelvin’s theorem. The differential rotation of the spiral vortex is represented by $\Omega(r)$; it should be noted that the asymptotic solution (A1) is fully determined when $\Omega(r)$ has been chosen under the constraint (A2b).

To obtain a full asymptotic solution, the vorticity (A1) is strained in the (z, r) plane and many such strained spiral vortex sheets are added together with the same center of the spiral and the same external strain. Finally one replaces the time t by a ‘‘strained time’’ $T(t)$ (see Lundgren [2,3]).

In this appendix, we first compute the radial and azimuthal components of the velocity field in one Lundgren strained spiral vortex sheet. The vorticity is given by (A1) and the axisymmetric straining flow field by (2.8a) and (2.8b) [$\psi(r, z) = (a/2)r^2z$ and $l=2$ as in the Burgers vortex]. In order to calculate the components u_r and u_ϕ of the fluid velocity at each point of the flow, we first calculate the stream function $\Psi(r, \phi, t)$ that corresponds to the unstrained 2D incompressible vortex sheet (A1); $\Psi(r, \phi, t)$ is related to the vorticity by

$$\omega = - \left(\frac{\partial^2 \Psi}{\partial r^2} + \frac{1}{r} \frac{\partial \Psi}{\partial r} + \frac{1}{r^2} \frac{\partial^2 \Psi}{\partial \phi^2} \right). \tag{A3}$$

The radial and azimuthal components of the velocity field around the Lundgren strained vortex sheet are given by

$$u_r = - \frac{ar}{2} + \frac{1}{r} \frac{\partial}{\partial \phi} \Psi(\sqrt{S(t)}r, \phi, T(t)), \tag{A4a}$$

$$u_\phi = - \frac{\partial}{\partial r} \Psi(\sqrt{S(t)}r, \phi, T(t)), \tag{A4b}$$

where the effects of the strain have been taken into account and where $S(t) = \exp[\int_0^t a(\tau) d\tau]$ is the stretch ratio and $T(t) = \int_0^t S(\tau) d\tau$ the strained time [see Lundgren [2,3]; the strain rate may be a function of time, i.e., $a = a(\tau)$].

Following Lundgren [2], we expand the vorticity and stream function in Fourier series in ϕ . The vorticity (A1) may be written

$$\omega(r, \phi, t) = f(r) \sum_{n=-\infty}^{+\infty} e^{in[\phi - \Omega(r)t]}, \tag{A5}$$

and the stream function

$$\Psi(r, \phi, t) \approx \Psi_0(r) + \frac{t^{-2}f(r)}{[d\Omega(r)/dr]^2} \left\{ \frac{\pi^2}{3} + \frac{1}{2} \left[\phi - \Omega(r)t - 2\pi \operatorname{int} \left(\frac{\phi - \Omega(r)t}{2\pi} \right) \right]^2 - \pi \left[\phi - \Omega(r)t - 2\pi \operatorname{int} \left(\frac{\phi - \Omega(r)t}{2\pi} \right) \right] \right\}. \tag{A11}$$

[By careful injection of (A11) into (A3) one can recover (A1).]

From (A4a) and (A11),

$$u_r \approx - \frac{ar}{2} + \frac{T(t)^{-2}f(\sqrt{S(t)}r)}{r\{(d\Omega/dr)[\sqrt{S(t)}r]\}^2} \left[\phi - \Omega(\sqrt{S(t)}r)T(t) - 2\pi \operatorname{int} \left(\frac{\phi - \Omega(\sqrt{S(t)}r)T(t)}{2\pi} \right) - \pi \right], \tag{A12a}$$

and from (A4b), (A11), and (A9) one obtains

$$\Psi(r, \phi, t) = \sum_{n=-\infty}^{+\infty} \Psi_n(r, t) e^{in\phi}. \tag{A6}$$

One can check that when $n \neq 0$,

$$\Psi_n(r, t) \approx \frac{t^{-2}f(r)}{n^2[d\Omega(r)/dr]^2} e^{-in\Omega(r)t} \tag{A7}$$

is an asymptotic ($t \rightarrow \infty$) solution of

$$f(r) e^{-in\Omega(r)t} = - \left(\frac{\partial^2 \Psi_n}{\partial r^2} + \frac{1}{r} \frac{\partial \Psi_n}{\partial r} - \frac{n^2}{r^2} \Psi_n \right), \tag{A8}$$

which is the Fourier-transformed version of (A3).

For $n=0$, (A8) and (A2b) imply (setting the additive constant to 0)

$$\frac{\partial \Psi_0}{\partial r} = -r\Omega(r). \tag{A9}$$

It follows that as $t \rightarrow \infty$,

$$\Psi(r, \phi, t) \approx \Psi_0(r) + \sum_{n \neq 0} \frac{t^{-2}f(r)}{n^2[d\Omega(r)/dr]^2} e^{in[\phi - \Omega(r)t]}. \tag{A10}$$

At this stage, one needs to sum a Fourier series of the type

$$\sum_{n \neq 0} \frac{e^{inx}}{n^2} = 2 \sum_{n=1}^{+\infty} \frac{\cos nx}{n^2},$$

and standard Fourier methods lead to

$$\sum_{n=1}^{+\infty} \frac{\cos nx}{n^2} = \frac{\pi^2}{6} + \frac{1}{4} \left[x - 2\pi \operatorname{int} \left(\frac{x}{2\pi} \right) \right]^2 - \frac{\pi}{2} \left[x - 2\pi \operatorname{int} \left(\frac{x}{2\pi} \right) \right],$$

where $\operatorname{int}(x/2\pi)$ is the integer value of $x/2\pi$. Consequently, (A10) may be summed up to give

$$u_\phi \approx S(t)r\Omega(\sqrt{S(t)}r) + O(T(t)^{-1}S(t)) \tag{A12b}$$

as $t \rightarrow \infty$. Note that there are contributions to u_r from both the strain-rate field and the spiral vortex sheet. Note also the jump in u_r across the sheet of vorticity at $\phi = \Omega(\sqrt{S(t)}r)T(t)$. A similar jump can be found in the $O(T(t)^{-1}S(t))$ term of u_ϕ associated with the spiral vortex sheet. The contribution of the induced velocity from the vortex sheet to u_r and u_ϕ tends to 0 as $t \rightarrow \infty$, and the azimuthal velocity is dominated by the differential rotation

$\Omega(\sqrt{S(t)}r)$ which rotates the entire sheet structure. Finally, note that the leading order in (A12) is axisymmetric, so that the flow tends towards axisymmetry as $t \rightarrow \infty$.

Lundgren [2] shows how the δ function in (A1) may be modified to account for nonvanishing viscosity and for $\omega(r, \phi, t)$ to be an asymptotic solution of the Navier-Stokes equations under the same condition (A2). Here we only deal with an inviscid Lundgren asymptotic solution which has a singularity in vorticity down to vanishing scales. This singularity is “complex” because of the *spiral accumulating* structure of the jumps in velocity which extends all the way to the spiral’s center. In fact, the Lundgren singularity is twofold: the spiral accumulation of the vortex sheet [see (A1)], and the simple singularity in $\Omega(r)$, since $\Omega(r)$ is monotonically increasing as $r \rightarrow 0$ [see (A2b)]. Such complex singularities are not included in the family of simple singularities that generate streamlines with $D_K = 1$ as we discussed in Sec. B A. Streamlines can exist with $D_K > 1$ in the Lundgren spiral vortex sheet. The strain rate is identical to the one in the Burgers vortex, and again severely limits the region of space where $D_K > 1$. In that restricted region, however, the D_K of streamlines is a direct reflection and a simple function of the Kolmogorov capacity of the Lundgren spiral vortex sheet and of the related singularity in $\Omega(r)$.

The equation $r = r(\phi)$ of a streamline’s projection on the (r, ϕ) plane may be obtained by integrating

$$\frac{d\phi}{dr} = \frac{u_\phi}{ru_r} \approx -\frac{4\pi\sqrt{S(t)}}{a} \frac{\Omega(\sqrt{S(t)}r)}{r}, \quad (\text{A13})$$

to leading order in time. Consequently, the vortex sheet and the projected streamline have the same spiral geometry. That geometry is a direct reflection of the differential rotation of the vortex sheet, and therefore, by virtue of (A2a), of how the ϕ -averaged vorticity $f(r)$ is radially distributed in space. If $\Omega(r) \sim r^{-\alpha}$, the projection of the streamline takes the spiral form $r(\phi) \sim \phi^{-1/\alpha}$, which is *the same spiral form adopted by the vortex sheet*. The Kolmogorov capacity of this spiral streamline projection is (Vassilicos and Hunt [4])

$$D_{K\text{proj}} = 1 + D'_K \quad (\text{A14a})$$

if the spiral has only a few turns, and

$$D_{K\text{proj}} = \max(1, 2D'_K) \quad (\text{A14b})$$

if the spiral has a large number of turns, where

$$D'_K = \frac{\alpha}{1 + \alpha}. \quad (\text{A14c})$$

The Kolmogorov capacity of the spiral vortex sheet is $1 + D_{K\text{proj}}$ because the number of boxes of size δ needed to cover the sheet is equal to the number of boxes of that size needed to cover the spiral intersection of the sheet with the plane normal to the z direction ($\propto \delta^{-D_{K\text{proj}}}$) times the number of boxes needed to cover the sheet along the z axis ($\propto \delta^{-1}$) (see the box-counting algorithm in Sec. III, and Vassilicos and Hunt [4]).

Note that $D_{K\text{proj}}$ is directly related to the power α that determines the radial fall off of the ϕ -averaged vorticity $f(r) \sim r^{-\alpha}$. If the radial decrease of $\Omega(r)$ is faster than any power law $r^{-\alpha}$, then $D_{K\text{proj}} = 2$ and the Kolmogorov capacity of the spiral vortex sheet is 3. The measure of the Kolmogorov capacity of a streamline around a strained spiral vortex sheet is therefore a measure of the vorticity variation radially within the vortex as well as of the Kolmogorov capacity of the spiral vortex sheet itself.

The Kolmogorov capacity of a 3D streamline is $D_K = 1$ if, after one turn of the spiral, the radial displacement Δr_n is smaller than the axial displacement Δz_n . This is indeed the case with the Lundgren vortex because of the persistent strain, unless the box-counting algorithm is limited to a region where $\Delta z_n \ll \Delta r_n$, in which case $D_K = D_{K\text{proj}}$. When $\Omega(r) \sim r^{-\alpha}$, $\Delta r_1 = r_0(1/a\alpha - 2\pi)^{1/2\alpha} - r_0$ and $\Delta z_1 = z_0(1/a\alpha - 2\pi)^{-1/\alpha} - z_0$, and the region where $D_K = D_{K\text{proj}}$ is bounded by

$$z_0 < r_0 \frac{(1/a\alpha - 2\pi)^{1/2\alpha} - 1}{(1/a\alpha - 2\pi)^{-1/\alpha} - 1}. \quad (\text{A15})$$

-
- [1] J. C. R. Hunt and J. C. Vassilicos, Proc. R. Soc. London, Ser. A **434**, 183 (1991).
 [2] T. S. Lundgren, Phys. Fluids **25**, 2193 (1982).
 [3] T. S. Lundgren, Phys. Fluids A **5**, 1472 (1993).
 [4] J. C. Vassilicos and J. C. R. Hunt, Proc. R. Soc. London, Ser. A **435**, 505 (1991).
 [5] O. Cadot, S. Douady, and Y. Couder, Phys. Fluids **7**, 630 (1995).
 [6] E. Villermeaux, B. Sixou, and Y. Gagne, Phys. Fluids **7**, 2008 (1995).
 [7] J. Jiménez, A. A. Wray, P. G. Saffman, and R. S. Rogallo, J. Fluid Mech. **255**, 65 (1993).
 [8] N. K.-R. Kevlahan and J. C. Vassilicos, Proc. R. Soc. London, Ser. A **447**, 341 (1994).
 [9] A. Vincent and M. Meneguzzi, J. Fluid Mech. **225**, 1 (1991).
 [10] J. M. Burgers, *Advances in Applied Mechanics* (Academic, New York, 1948), Vol. I.
 [11] P. K. Yeung and J. G. Brasseur, Phys. Fluids A **3**, 884 (1991).
 [12] P. K. Yeung and S. B. Pope, J. Comput. Phys. **79**, 2 (1988); **79**, 373 (1988).
 [13] S. Balachandar and M. R. Maxey, J. Comput. Phys. **83**, 1 (1989); **83**, 96 (1989).
 [14] B. B. Mandelbrot, *The Fractal Geometry of Nature* (Freeman, New York, 1982).